UC Riverside

UC Riverside Electronic Theses and Dissertations

Title

Heat Transport and Spin Accumulation in Nanoscale Metal Multilayers

Permalink

https://escholarship.org/uc/item/2589j4s4

Author

Gomez, Michael

Publication Date

2019

Peer reviewed|Thesis/dissertation

UNIVERSITY OF CALIFORNIA
RIVERSIDE

Heat Transport and Spin Accumulation in Nanoscale Magnetic Multilayers

A Dissertation submitted in partial satisfaction
of the requirements for the degree of

Doctor of Philosophy

in

Materials Science and Engineering

by

Michael Joseph Gomez

June 2019

Dissertation Committee:
Dr. Richard B. Wilson, Chairperson
Dr. Ashok Mulchandani
Dr. Sinisa Coh

The Dissertation of Michael Joseph Gomez is approved:

_____

_____

_____

Committee Chairperson

University of California, Riverside

ACKNOWLEDGEMENTS

I want to thank the many people who have helped me achieve all that I have, though the list of names would be so vast that these pages could not contain them. That being said, I must still mention those that have lifted me up with such efforts that I may reach greater heights if only through their undeniable presence. First I thank Richard Wilson, whom without I may as well have sought my PhD in a bowl of alphabet soup. Through my shortcomings, my ignorance, and my unyielding desire to sleep, I have come to know very well the passion for science that drives Richard. If nothing else, though in truth much much else, having witnessed Richard in his element has produced a vision of clarity within me that has permeated my character. For this and all of Richard's guidance, I am truly grateful.

I also thank my family and friends who supported me through my oddities and insanities and profanities. I thank my father, Mike Gomez, for providing a platform from which I could grow, reluctant as I may have been to do so (See unyielding desire to sleep). Finally I thank my closest friend, Cindy Merida. Cindy who helped me to assemble a resume and lift my spirits in times of dread, who laughed with me in moments of hysteria, who physically pushed me from desk to vacuum chamber as I sat in a rolling office chair when, though exhaustion, walking was no longer a mentionable topic, and who overcame the abyss alongside me. Thank you.

ABSTRACT OF THE DISSERTATION

Heat Transport and Spin Accumulation in Nanoscale Magnetic Multilayers

by

Michael Joseph Gomez

Doctor of Philosophy, Graduate Program in Materials Science and Engineering
University of California, Riverside, June 2019
Dr. Richard B. Wilson, Chairperson

Understanding heat transport in metal multilayers on nanometer length scales and picosecond time scales after femto-second laser heating is important for a wide variety of scientific fields, including ultrafast magnetism, spin caloritronics, photocatalysis, and many more. Understanding spin-transport in magnetic systems following laser excitation is important for the burgeoning field of THz spintronics. Currently, the mechanisms are not well understood for how heat and spin are transported in nanoscale magnetic systems on ultrafast time-scales.

The goal of my thesis research is to develop new experimental methods for studying heat-transfer and spin-transfer in nanoscale magnetic multilayers. My research can be divided into five categories. First, I designed and built a TDTR and TR-MOKE pump/probe system capable of wavelength dependent scans. Second, I characterized interfacial spin-currents between Au layers and adjacent iron-garnet insulators with magnetic order. Third, I showed that wavelength dependent thermoreflectance experiments on Au allow for independent measurements of electron vs. phonon temperatures. Fourth, I characterized heat-transfer in Au/Co multilayer systems. Finally, fifth, I characterized spin-transport across Au/Co multilayer systems.

I also investigate spin-transport in Au/magnetic insulator bilayer systems. Typically, these systems are investigated indirectly via transverse charge currents and then the coefficient of interest, such as the spin dependent Seebeck coefficient, is related back to the charge current via secondary effects, such as the inverse spin Hall effect. In order to describe this Au/magnetic insulator system more completely, I utilize a variety of time-domain thermoreflectance and time-resolved magneto optic Kerr effect measurements to more completely investigate the processes.

Thermoreflectance measurements and predictions typically rely on the assumption that electrons and phonons in the metal are in thermal equilibrium. I conduct wavelength dependent TDTR measurements of a thin Au film. These measurements show that electron and phonon contributions to the thermoreflectance are wavelength dependent. Therefore, wavelength-dependent TDTR allows for phonon specific or electron specific thermometry of Au systems.

Through a combination of wavelength dependent time domain-thermoreflectance (TDTR) and time-resolved magneto optic Kerr effect (TR-MOKE) measurements, I provide insight into the complicated heat transport behavior in nanoscale metal systems. An important result of my work is the development of new experimental methods for studying how photoexcited electrons transport energy with respect to penetration depth into the sample as well as the nonequilibrium between electrons and phonons in nanoscale Au multilayer systems. As it stands, the transport behavior of hot electrons after femtosecond laser heating is still debated. Specifically, it is not currently possible to predict whether hot electrons transport energy ballistically (travel near the Fermi velocity), or transport energy diffusively (related to the materials diffusivity) diffusive transport. Electron-electron, electron-phonon, and phonon-phonon interactions produce a complicated set of scattering events. By using several TDTR and TR-MOKE experiments and by fitting the experimental results with a thermal model, I am able to describe the distance hot electrons travel in the first few picoseconds after photoexcitation as neither ballistic nor diffusive, but rather superdiffusive.

Spin accumulation in metals is not yet completely described. Typical methods for measuring spin accumulation are indirect, in that they measure secondary electrical effects and then relate them back to the phenomena of interest, e.g. the inverse spin hall effect. I use TR-MOKE measurements to directly measure spin injections into Au films due to demagnetization of adjacent magnetic metal or magnetic insulator materials. Finally, I report measurements of the Kerr angle of Au as a function of wavelength. My experimental measurements of the Kerr angle vs. wavelength are in reasonable agreement with theory.

TABLE OF CONTENTS

Chapter 4: Heat Transport in Nanoscale Metal Multilayers

Chapter 5: Spin Accumulation in Au

LIST OF FIGURES

Chapter 1

Chapter 2

Chapter 3

Chapter 4

Chapter 5

LIST OF TABLES

Chapter 2

Chapter 3

Introduction

Hot electron dynamics in metals after femtosecond laser excitation have been of great interest for several years, with technological developments in ultra-fast pulsed lasers in the late 1980s spawning an era of ultra-fast pump-probe spectroscopy research. One focus of these pump-probe experiments was the thermal relaxation of the hot electrons in a metal system. In these pump-probe experiments, an ultra-fast laser pulses excite the metal's electrons into a non-equilibrium distribution. These hot electrons scatter with electrons and phonons until the electrons are in thermal equilibrium with the phonons, after which the excess energy deposited by the ultra-fast laser pulse diffuses into the substrate. With the goal being to describe the thermal relaxation of the hot electrons separate from other effects, in 1987 Phil Allen [1] derived a microscopic model for describing the thermal relaxation coupling constant, g_{ep}, used in the heat diffusion eq. 1. The electron-phonon energy transfer coefficient g_{ep} describes the transfer of energy between the hot electrons and the phonons

$$C_e \frac{dT_e}{dt} = g_{ep}(T_p - T_e). \qquad (1)$$

This microscopic description of the coupling constant promoted experimental investigation into the coupling constant via pump-probe techniques in nm thick metal films[2-4]. In addition to several studies on how hot electrons relax in thin-metal films, experiments were carried out to investigate how hot electrons carried energy across thick Au metal layers. Brorson *et al.* performed pump probe experiments on Au layers of varied thickness and measured how long heat took to arrive on one side after laser excitation of the other. They concluded that heat transport in Au layers between 20nm and 300nm was ballistic because the hot electrons travelled near the Fermi velocity. Furthermore, the time-scale for heat arriving on the opposite end of the Au film scaled linearly with increasing Au thickness [2].

Though the problem of transport in Au layers has been studying for decades, the behavior of heat transport in nm thick metals on ultra-fast time scales following photo-excitation remains unclear[5-6]. Complex electron-electron, electron-phonon, and phonon-phonon scattering proves to be a difficult task to describe following ultra-fast laser pulse heating leading to complications in heat transport descriptions.

Recently there has been a resurgence of interest regarding describing heat transport in nanoscale metal multilayers due to several discoveries in the fields of ultrafast magnetism and spintronics [6-12]. Demagnetization of a nanoscale magnetic multilayer via an ultra-fast laser pulse was shown to inject a spin current into an adjacent non-magnetic metal with applications relating to non-volatile magnetic memory [7]. Optically driven spin currents have been shown to produce emission of previously elusive THz radiation ranging from 1-30THz due to ultra-fast heating of magnetic multilayers [8]. Ultra-fast optical switching in magnetic multilayers was shown following laser pulse heating in which a single femtosecond pulse was able to reverse the magnetization of a magnetic film on picosecond time-scales[9]. Understanding all of these phenomena requires knowledge of whether heat transfer in a metal multilayer is diffusive or ballistic. However, no clear criteria currently exist for determining when and why heat transfer is diffusive vs. ballistic in a metal after laser excitation.

In parallel with the discoveries described above, several recent experiments have provided new insight into heat transfer in bilayer and multilayer systems, e.g. Au/Pt bilayers 100ps [13-15] . These studies discovered that heat-transfer is more complex and interesting in multilayer samples than single thin-film samples. For example, while the time-scales needed for electrons to thermalize with phonons is less than 1 ps in most single element thin-films, it may be as long as 100ps [13-15] in metal multilayers. The ability of electrons with different spin further complicates transport in magnetic materials. Up and down electrons have different mobilities and

thermal transport properties [16-17]. Disagreement between transport behavior persists as the debate as to whether heat is transported ballistically, diffusively, or super-diffusively and the degree to which hot electron transport is responsible for the ultra-fast magnetization dynamics following ultra-fast laser pulse heating is unknown [2, 5-6, 18-21].

In order to better understand the heat transport behavior in these nanoscale magnetic multilayer systems, new experimental methods are needed to measure how far hot electrons transport energy. Additionally, new methods for optically detecting spin currents will improve understanding of spin transport in nanoscale systems on ultrafast time-scales. My PhD work focuses on the development of such experimental methods. I also present the experimental studies that advance the state of the art in the four areas listed below.

My PhD work aims to resolve four gaps in understanding related to ultra-fast heat transport:

1. How far can photo-excited hot electrons transport energy following femtosecond laser excitation in nanoscale magnetic multilayers?

2. Can we use wavelength dependent thermoreflectance measurements to distinguish between electron vs. phonon temperature rises in Au systems?

3. What are the microscopic origins of the spin Seebeck effect, i.e. the generation of spin-current due to temperature gradients in nanoscale metal/magnetic-insulator heterostructures?

4. What are the magneto-optic properties of Au in the presence of spin-accumulation and how do they depend on wavelength?

In order to resolve these gaps, I built a time-domain thermoreflectance (TDTR) and time-resolved magneto optic Kerr effect (TR-MOKE) pump/probe apparatus. The apparatus can perform measurements as a function of position, probe energy, and thickness of metal layer. In

short, I designed a series of experiments that can measure how heat and spin evolve in space and time on nm length and ps time scales.

The first experiments I performed with the pump/probe system focused on the origins of thermoreflectance in Au. After a femtosecond laser pulse is absorbed by the metal's electrons, the temperature of the Au electrons and phonons increase. Changes in the reflectance of the metal after ultra-fast heating are proportional to the change in temperature. In chapter 3, I show that time-domain thermoreflectance measurements of a thin Au film as a function of probe wavelength allows for independent measurements of the electron temperature and the phonon temperature.

I used time-resolved magneto optic Kerr effect measurements in my other three experimental studies. MOKE stands for the magneto-optic Kerr effect. MOKE describes a small rotation of the polarization that occurs when light reflects from a magnetic material. The amount of polarization rotation is proportional to the magnetic moment of the material. In a non-magnetic material, such as Au, MOKE is a sensitive probe of spin-accumulation that occurs due to spin injection from adjacent layers.

The first TR-MOKE experiments I performed focused on using MOKE as a thermometer. I studied heat transfer in Au-Co multialyers that consisted of 4 alternating layers of Au and Co ~ 1nm thick, followed by an optically thick layer of Au between 90 and 300 nm thick. I optically excited the Au surface with a pump laser pulse. I monitored the temperature of the Co as a function of time via MOKE measurements. The magnetic moment of the Co is temperature dependent. Therefore, by measuring the change in magnetization of Co, I can monitor how much energy arrives at the Au/Co multilayer from the opposite Au surface. I conducted experiments as a function of Au thickness, varying the Au from 90 to 230 nm thick. We also explored how changing the Au transport layer to Cu effected results. I found that in Au the hot electrons travel ~60 nm further than diffusive theory predicts, which may be a signature of superdiffusive transport. In Cu, hot

electron transport is significantly different than in Au despite similar thermal properties. The differences between Au and Cu demonstrate the necessity of using microscopic transport models for describing energy transfer in nanoscale metal systems.

I studied spin-injection from two types of systems: Au/iron-garnet bilayers and Au-Co multilayers. First, I describe our experiments on Au-Co multilayers. The Au-Co multialyers consisted of 4 alternating layers of Au and Co ~ 1nm thick, followed by an optically thick layer of Au between 90 and 300 nm thick. The primary goal of these experiments was to measure how the Kerr angle of Au depends on wavelength. A secondary goal was to measure the distance spin can diffuse across Au layers. In these experiments, we heat the Co layers with our pump laser. This ultrafast heat generates a spin-current. Spin diffuses across the Au layer. We detect the spin accumulation at the Au surface (opposite end of the sample to the Co layer). By repeating these experiments as a function of probe energy, we measure the Kerr angle of Au vs. wavelength. My work on optical detection of spin accumulation in Au provides insights to spin transport on nm length scales and ps time scales, as well as corroborating theory predictions.

I also used MOKE to study the microscopic origins of the spin Seebeck effect. These experiments focused on 60 nm Au / iron-garnet bilayers. Similar to the AuCo experiments, ultrafast heating results in a spin-current. However, changing the spin source from a magnetic metal multilayer to a magnetic insulator layer, such as a rare earth doped iron garnet, results in a different spin injection mechanism. Spin-current between Au and a magnetic insulator is governed by temperature gradients. At equilibrium, constant annihilation and creation of magnons across the Au/iron garnet interface is taking place due to metal electron and magnetic insulator magnon coupling. Electrons in the metal colliding with the interface can either create or absorb a magnon from the magnetic insulator. This interaction flips electron spins. At equilibrium, the creation and annihilation of magnons results in no net spin accumulation in the Au. After laser absorption, a

temperature difference between the Au/iron garnet interface removes the system from equilibrium, increases the rate of magnon emission, and causes spin to accumulate in the Au layer on ps time scales. The generation of a spin current due to a temperature gradient is called the spin-dependent Seebeck effect (SSE). Typically the SSE is measured via secondary effects, such as the inverse spin Hall effect (ISHE), and a charge current is then related to a spin current. Ideally the SSE would be investigated directly, and described fully. I use TDTR to measure the temperature gradients and thermal transport properties. I use TR-MOKE to measure the spin accumulation into the Au that results from these temperature gradients. The Spin Seebeck coefficient varies by a factor of three for Au/TmIG, Au/TbIG, Au/EuIG, and Au/YIG systems. It is largest in Au/TmIG. My experiments suggest that the magnitude of the SSE is dominated by interfacial properties, and not the magnetic properties of the garnets themselves.

References

1.   Allen, P.B., *Theory of thermal relaxation of electrons in metals.* Physical review letters, 1987. **59**(13): p. 1460.

2.   Brorson, S., J. Fujimoto, and E. Ippen, *Femtosecond electronic heat-transport dynamics in thin gold films.* Physical Review Letters, 1987. **59**(17): p. 1962.

3.   Fann, W., et al., *Electron thermalization in gold.* Physical Review B, 1992. **46**(20): p. 13592.

4.   Brorson, S., et al., *Femtosecond room-temperature measurement of the electron-phonon coupling constant γ in metallic superconductors.* Physical Review Letters, 1990. **64**(18): p. 2172.

5.   Bergeard, N., et al., *Hot-electron-induced ultrafast demagnetization in Co/Pt multilayers.* Physical review letters, 2016. **117**(14): p. 147203.

6.   Choi, G.-M., et al., *Thermal spin-transfer torque driven by the spin-dependent Seebeck effect in metallic spin-valves.* Nature physics, 2015. **11**(7): p. 576.

7.   Melnikov, A., et al., *Ultrafast transport of laser-excited spin-polarized carriers in Au/Fe/MgO (001).* Physical review letters, 2011. **107**(7): p. 076601.

8.   Seifert, T., et al., *Efficient metallic spintronic emitters of ultrabroadband terahertz radiation.* Nature photonics, 2016. **10**(7): p. 483.

9.   Gorchon, J., et al., *Single shot ultrafast all optical magnetization switching of ferromagnetic Co/Pt multilayers.* Applied Physics Letters, 2017. **111**(4): p. 042401.

10.   Kimling, J., et al., *Picosecond spin Seebeck effect.* Physical review letters, 2017. **118**(5): p. 057201.

11.   Graves, C. E., et al. "Nanoscale spin reversal by non-local angular momentum transfer following ultrafast laser excitation in ferrimagnetic GdFeCo." *Nature materials* 12.4 (2013): 293.

12.   Mangin, Stéphane, et al. "Engineered materials for all-optical helicity-dependent magnetic switching." *Nature materials* 13.3 (2014): 286.

13.   Choi, Gyung-Min, R. B. Wilson, and David G. Cahill. "Indirect heating of Pt by short-pulse laser irradiation of Au in a nanoscale Pt/Au bilayer." *Physical Review B* 89.6 (2014): 064307.

14.   Wang, Wei, and David G. Cahill. "Limits to thermal transport in nanoscale metal bilayers due to weak electron-phonon coupling in Au and Cu." *Physical review letters* 109.17 (2012): 175503.

15.   Pudell, J., et al. "Layer specific observation of slow thermal equilibration in ultrathin metallic nanostructures by femtosecond X-ray diffraction." *Nature communications* 9.1 (2018): 3335.

16.   Kimling, Johannes, and David G. Cahill. "Spin diffusion induced by pulsed-laser heating and the role of spin heat accumulation." *Physical Review B* 95.1 (2017): 014402.

17.   Kimling, Johannes, et al. "Spin-dependent thermal transport perpendicular to the planes of Co/Cu multilayers." *Physical Review B* 91.14 (2015): 144405.

18.   Rudolf, Dennis, et al. "Ultrafast magnetization enhancement in metallic multilayers driven by superdiffusive spin current." *Nature communications* 3 (2012): 1037.

19.   Schellekens, A. J., et al. "Investigating the contribution of superdiffusive transport to ultrafast demagnetization of ferromagnetic thin films." *Applied Physics Letters* 102.25 (2013): 252408.

20.   Eschenlohr, A., et al. "Ultrafast spin transport as key to femtosecond demagnetization." *Nature materials* 12.4 (2013): 332.

21.   Battiato, Marco, Karel Carva, and Peter M. Oppeneer. "Superdiffusive spin transport as a mechanism of ultrafast demagnetization." *Physical review letters* 105.2 (2010): 027203.

CHAPTER 1

Experimental Methods

High Sensitivity Pump-Probe Measurements of Magnetic, Thermal,
and Acoustic Phenomena with a Spectrally Tunable Oscillator

We describe an optical pump/probe system for sensitive measurements of time-resolved optical measurements of material dynamics. The instrument design is optimized for time-resolved magneto-optic Kerr effect (TR-MOKE) measurements of dynamics in magnetic materials. The system also allows for time-domain thermoreflectance (TDTR) measurements of thermal transport properties, and picosecond acoustic measurements of film thickness and/or elastic constants. The system has several advantages over the conventional design for TR-MOKE and/or TDTR systems. Measurements of pump-induced changes to the probe beam intensity are shot-noise limited, corresponding to a nanoradian noise floor in MOKE experiments. Furthermore, the wavelengths of the probe beam are straightforward to tune between 350-530 and 690-1060 nm. A tunable wavelength allows for optical resonances in a wide array of materials to be excited and/or probed. The setup is calibrated to allow for the real and imaginary components of Kerr signals to be separately quantified. Finally, the system's design allows for MOKE and/or thermoreflectance measurements of both sides of a sample. Pumping and probing the sample on opposite sides allows time-of-flight measurements of transport phenomena in nanoscale films.

I. Introduction. — Pump/probe instruments are common tools for characterizing dynamics of materials. In a typical pump-probe experiment, an optical pump pulse excites the sample. The time-evolution of the excitation is recorded by measuring changes in optical properties with a time-delayed probe pulse. In a time-resolved magneto optic Kerr effect measurement, the probe pulse indirectly detects changes in magnetization of a magnetic material via changes in the polarization of the reflected probe pulse. In a time-domain thermoreflectance experiment, the probe pulse measures temperature induced changes in the reflectance of a thin-metal film. Pump-probe apparatuses are often designed to operate in a narrow spectral region, e.g. near 800 nm where emission from Ti:Sapphire lasers is a maximum [1-10].

An ability to tune the wavelength of the probe and/or pump laser is desirable for several reasons. A tunable probe wavelength can allow additional information to be extracted from pump/probe experiments that is not otherwise possible. Hot carrier energy distributions in Au can be extracted from wavelength dependent TDTR measurements [11]. Wavelength dependent TR-MOKE measurements of ferrimagnetic TbFeCo thin metal films allow for an independent determination of the magnetization dynamics of the rare-earth vs. transition-metal magnetic sublattices [12]. Another advantage of laser wavelength tunability is signal strength. In both TDTR and TR-MOKE experiments, probe signal levels are typically small. For example, consider a time-resolved magneto optic Kerr effect measurement of a thin film of magnetic metal. The Kerr angle, i.e. the difference in polarization between reflected and incident light, is on the order of 1 mrad. If the pump beam induces a 1% change in magnetization, the probe signal of interest will be ~ 10^{-5} of the total. Probe signal levels are comparable in time-domain thermoreflectance experiments [2]. Pump induced temperature changes in metal films are typically on the order of 1 K, and the thermoreflectance of most metals is on the order of 10^{-5} K^{-1} [2].

Tuning the probe wavelength to optical resonances of the sample can significantly increase the signal strength in a pump/probe experiment. The Kerr angle in Au/Co multilayers varies by as much as a factor of 15 between 1.5 and 5 eV [13]. Many magnetic insulators have negligible Kerr angles at infrared wavelengths, but large magneto-optical responses at energies above their band gap, e.g. above 2.5 eV in yttrium iron garnet [14].

An ability to tune laser wavelength in a pump-probe experiment is helpful for picosecond acoustic measurements. TDTR and TR-MOKE experiments often rely on picosecond acoustic measurements of the metal film thickness to analyze the data [3]. Picosecond acoustic measurements use strain-induced changes in reflectivity of a metal film to measure the time for a pump-induced sound wave to traverse the film [15]. Since the speed-of-sound in metals is typically known, this allows an accurate determination of the film thickness. Unfortunately, the reflectance of many metals is not sensitive to strain at all wavelengths. For example, picosecond acoustic signals are negligible in Au and Cu in the near infrared, but large at interband transitions near 2 eV [16].

Here, we provide details of a pump/probe instrument design that takes advantage of the wavelength tunability of commercially available Ti:Sapphire oscillators. The rest of the paper is organized as follows. In section II, we provide the details of our experimental setup and provide a Jones matrix analysis of the MOKE signals we detect in our apparatus. In section III we provide examples of TDTR, picosecond acoustic, and TR-MOKE data acquired with the instrument.

II. Experimental Setup. — The pump/probe system is shown in Fig. 1.1. The setup is built around a Mai-Tai Ti:Sapphire oscillator. The laser wavelength is tunable between 690 and 1060 nm. The average output of the oscillator power is 1.8 W at 690 nm, 2.88 W at 800 nm, and 0.9W at 1060 nm. The setup is designed for experiments with both red (690-1060 nm) or blue (350-530 nm) pump and probe beams, i.e. red-pump/red-probe, red-pump/blue-probe, blue-pump/blue-probe, or

blue-pump/blue-probe. Two of these four possible configurations are shown in Fig. 1.1: red-pump/red-probe and red-pump/blue-probe.

The laser passes through two collimating lenses to increase the beam size to ~ 4 mm and reduce divergence. A 4 mm beam size is small enough to simplify alignment down-stream through the Faraday isolator and Electro-Optic-Modulator. After the lenses, we use two mirrors to change the height of the beam from 3 inches to 5.5 inches above the optical table. The beam height remains at 5.5 inches throughout the rest of the setup. Next, the beam passes through a broadband half wave-plate and a broad-band Farady isolator. The half-wave plate, together with the polarizing beam splitter on the input of the Faraday isolator, allows us to reduce the laser beam power. The isolator also prevents back reflections from destabilizing the oscillator. We use a half wave-plate and polarizing beam splitter pair to divide the laser into pump and probe beams.

Pump Beam Path. The pump beam is modulated with a 50% duty cycle at frequency f_{mod} with an electro-optical modulator (Conoptics 350-160 with model 25D driver). After the electro-optic modulator, we use a 3x beam expander to increase the diameter of the pump beam to 7 mm before the delay stage. This is necessary because the beam divergence of a gaussian laser is inversely related to the beam waist. The delay stage changes the path length of the pump beam. Without reducing the divergence, the change in path length would result in the pump beam spot-size that changes with delay-time, which is undesirable for stroboscopic experiments. After the beam expander, the pump beam bounces of two retroreflectors that are mounted on a 1 m long mechanical delay stage. This allows a change in pump path length of 4 m, corresponding to a change in delay time of 13.34 ns. A delay time that spans the full 12.5 ns delay between laser pulses allows for analysis of the

After the delay stage, the pump beam takes one of two paths, depending on the wavelength desired. If the experiment requires a pump wavelength between 350 and 530 nm, a mirror on a

kinematic mount diverts the pump beam through a home-built second harmonic module. The module consists of two lenses and a BBO crystal. After the module, the pump passes through a low-pass optical filter and is directed towards the piezo mirror. For experiments that require a pump wavelength between 690 and 1060 nm, the pump beam is directed directly towards the piezo mirror after the delay stage without passing through the SHG module.

The piezo-mirror that allows for computer control of the angular displacements. The piezo-mirror works together with two lenses and an objective lens. The objective lens focuses the pump onto the sample surface. The location on the sample where the beam is focused onto depends on the angle the pump beam impinges on the objective lens. Therefore, the piezo-mirror and two lenses allow the position of pump beam to be rapidly scanned on the sample surface without optical aberrations changing the size and/or shape of the focused beam.

Probe Beam Path. After being separated from the pump beam by the polarizing beam splitter after the Faraday isolator, the probe beam passes through two lenses that expand the beam to 7mm to prevent divergence. Then, the probe beam passes through a second-harmonic generation module. The second harmonic module converts doubles the frequency, i.e. converts the 690 – 1060 nm beam into 345 – 530 nm beam. The second harmonic module consists of a half-wave-plate, a focusing lens, a 2mm lithium triborate crystal on a rotation stage, a collimating lens, and a dichroic mirror to separate the fundamental from the frequency doubled light. When the probe beam passes through the lithium triborate crystal at normal incidence, the conversion efficiency is a maximum when the probe wavelength is 865 nm. For higher (lower) probe wavelengths we rotate the lithium triborate crystal clock-wise (counter clockwise) about it's z-axis until the second harmonic power is a maximized. The conversion efficiency at 690, 800, and 1060 nm for an input power of 0.5 W is 10, 15, and 12%. After the SHG module, we include two lenses to remove divergence from the module. After the lenses, the probe beam is between 4 and 5 mm for 350 to 530 nm light.

If the desired probe wavelength is in the infrared, we insert two mirrors mounted on kinematic mounts so that the probe beam bypasses the second harmonic module, shown in Fig. 1.1. In this case, the probe spot-size is 4 to 5 mm for 690 to 1060 nm light.

The probe beam is directed towards the sample and objective lens with a non-polarizing beam splitter. The probe beam is focused on the sample with the objective lens. We use the piezo-mirror to move the pump beam across the sample surface until the pump and probe beam are overlapped, for confocal microscopy setup see Fig. 1.2. While Fig.1.2b shows our beam-offset experimental results and gaussian fit for the x and y directions of the beam overlap, in which the w_0 radius at $\frac{1}{e^2}$ of the maximum signal.

The probe path length is ~3.75 meters shorter than the pump path length, corresponding to a phase shift of 12.5 ns. This has no effect on the measurement since the rep-rate of the probe pulses is 80 MHz and the laser's phase jitter is much less than the pulse duration.

Signal Detection. Fig.1.1 shows the detection path for red vs. blue probe light. On the detection line, an optical filter blocks the pump light. After passing through a Soleil-Babinet Compensator (Thorlabs SBC-VIS) and broadband half-wave plate, the probe beam is split into orthogonal polarizations of light via a half-wave plate and Woolaston prism combination. After reflecting from a knife-edge right-angle prism mirror, each polarization is focused onto one of two inputs of a balanced amplified Si photodetector (Thorlabs 450A-AC). The photodetector outputs three voltages. V_1, V_2, and V_{RF}. The monitor outputs V_1 and V_2 are proportional the optical powers on each of the two inputs. The monitor output V_{RF} is proportional to the difference in two optical outputs. The V_{RF} output has a bandwidth is 100 Hz to 150 MHz, and therefore excludes the unmodulated CW component of the optical signal.

For TDTR experiments, the half-wave plate is rotated so that the full reflected probe beam intensity is focused on only one input. The balanced detector output V_{RF} is proportional to the reflectance of the sample. The RF-output is sent to a radio-frequency lock-in (SRS 844), which detects pump-induced changes in the reflectance at pump modulation frequency f_{mod}.

For TR-MOKE experiments, the signal of interest is related to the polarization of the reflected probe beam. The interaction of the probe beam with the sample, optical elements in the detection line, and half-wave-plate is described by the vector equation

$$
\begin{bmatrix} E_x \\ E_y \end{bmatrix} = T_o \left[\mathbf{HWP}\right]\left[\mathbf{C}\right]\left[\mathbf{S}\right] \begin{bmatrix} E_0 \\ 0 \end{bmatrix} = -iT_0 \begin{bmatrix} \cos\theta & \sin\theta \\ \sin\theta & -\cos\theta \end{bmatrix} \begin{bmatrix} 1 & 0 \\ 0 & \exp(-i\gamma) \end{bmatrix} \begin{bmatrix} r_p & r_{ps} \\ r_{sp} & r_s \end{bmatrix} \begin{bmatrix} E_0 \\ 0 \end{bmatrix},
$$

(1)

where $\left[\mathbf{S}\right]$ and $\left[\mathbf{HWP}\right]$ are the Jones matrix for the sample and half-wave plate, and θ is the angle between the half-wave plate's fast axis and the horizontal direction x. T_o accounts for the transmission of the optical components between the sample and detector that do not affect the relative phase of the x and y components of the electric field. In our setup $T_o \approx 0.9$. Finally, $\left[\mathbf{C}\right]$ is a Jones matrix to account for the phase retardation caused by the reflection from optical components between the sample and the half-wave plate. This matrix includes the effect of the compensator, as well as the phase change from 45° reflections from optical elements with multilayer dielectric coatings, such as broad-band beam splitters and mirrors, is significant and depends strongly on wavelength.

During MOKE measurements, the half-wave plate is rotated to $\theta \approx \pi/4$ so that the horizontal and vertical components are roughly equal. The Woolaston prism divides x and y components and diverts them towards the two inputs balanced photodiode. The monitor outputs generate a voltage of

$$\begin{bmatrix} V_1 \\ V_2 \end{bmatrix} = \frac{T_o \Re_{\mathbf{M}} I_i}{2} \begin{bmatrix} r_{pp}r_{pp}^* + r_{pp}r_{sp}^* \exp(i\gamma) + r_{sp}r_{pp}^* \exp(-i\gamma) + r_{sp}r_{sp}^* \\ r_{pp}r_{pp}^* - r_{pp}r_{sp}^* \exp(i\gamma) - r_{sp}r_{pp}^* \exp(-i\gamma) + r_{sp}r_{sp}^* \end{bmatrix}, \qquad (2)$$

where I_i is the intensity of the probe power incident on the sample surface, and $\Re_{\mathbf{M}}$ is the responsivity of the monitor outputs. The output of the RF photodiode is proportional to the difference in the optical power on each input,

$$V_{RF} = \Re_{RF} T_o I_i \left(r_{pp}r_{sp}^* \exp(i\gamma) + r_{pp}^* r_{sp} \exp(-i\gamma) \right), \qquad (3)$$

where $\Re_{RF}$ is the responsivity of the RF output, which is roughly a factor of 2 lower than $\Re_{\mathbf{M}}$ in our detector. Next, we rewrite Eq. (2) and Eq. (3) with the Fresnel reflection coefficients in polar form, $r_{pp} = |r_{pp}| \exp(i\phi_{pp})$ and $r_{sp} = |r_{sp}| \exp(i\phi_{sp})$, and assume $|r_{sp}| \quad |r_{pp}|$. This yields

$$V_1 \approx V_2 \approx T_o |r_p|^2 I_i \Re_{\mathbf{M}} / 2, \qquad (4)$$

and

$$V_{RF} = 2\Re_{RF} I_i |r_{pp}||r_{sp}| \left[\cos(\phi_{sp} - \phi_{pp}) \cos(\gamma) + \sin(\phi_{sp} - \phi_{pp}) \sin(\gamma) \right]. \qquad (5)$$

The quantity of interest in a MOKE measurement is the complex Kerr angle,

$$\Theta_K = \theta_k + i\varepsilon_k = r_{sp}/r_p = |r_{sp}|/|r_p| \left(\cos(\phi_{sp} - \phi_{pp}) + i\sin(\phi_{sp} - \phi_{pp}) \right). \qquad (6)$$

In a polar MOKE geometry (probe incident at normal incidence), both θ_k and ε_k are proportional to the magnetic moment in out-of-plane direction. Comparing Eqs. (4-6), we see that the RF monitor outputs a signal equal to

$$V_{RF} \approx 4V_1 \frac{\Re_M}{\Re_{RF}} \left[\cos(\gamma)\theta_k + \sin(\gamma)\varepsilon_k \right]. \qquad (7)$$

Inspection of Eq. (7) indicates that our signal measures the real part of the Kerr angle for $\gamma = 0$ and the imaginary part for $\gamma = \pi / 2$. The MOKE signal measured by the balanced detector will be maximized when $\gamma = \tan^{-1}\left(\varepsilon_k / \theta_k\right)$.

The phase change from 45° reflections from optical elements with multilayer dielectric coatings is significant and depends strongly on wavelength. We measured the value of γ from the optical elements on the detection path prior to the compensator and half-wave plate with a rotating quarter wave plate polarimeter.

The inclusion of the compensator on the detection line allows us to control the value of γ. Control of γ provides several advantages. It allows us to independently determine θ_k and ε_k vs. wavelength of our samples. For samples with multiple magnetic layers, adjusting γ allows us to isolate the magneto-optic signal from distinct layers, as outlined in Refs. [17] and [18].

The final step of signal detection is lock-in amplification. The RF-output of the balanced detector is sent to a radio-frequency lock-in (SRS 844), which detects pump-induced changes in the MOKE signal at the pump modulation frequency f_{mod}. We use low pass electric filters to remove unwanted frequency components that arise due to the square wave modulation of the pump beam. The in-phase and out-of-phase signals measured by the RF-lockin are outputted to two computer-based audio frequency lock-in amplifiers (NI model number of DAQ card). The audio frequency lock-ins are synchronized to the 200 Hz frequency of the mechanical chopper in the path of the probe beam. This removes background signals created by coherent rf pickup. The in-phase and out-of-phase signals are reported to a LabVIEW interface that also controls the delay line. The signals are recorded as a function of delay time between the pump and probe beams.

III. Experimental Results. — To test the effect of changing the probe wavelength in our measurements, we performed three sets of experiments on three types of samples. We performed

wavelength-dependent TDTR measurements of a thin 60 nm Au film on sapphire, wavelength-dependent MOKE measurements of a Au/Co multilayer on sapphire, and picosecond acoustic measurements of Au and Cu multilayer samples.

All samples were prepared via dc magnetron sputter deposition on c-cut sapphire substrates with an AJA Orion sputter system. The base pressure of the sputtering chamber is less than 5 x 10^{-8} torr. During sputtering, a mass flow controller connected to high purity argon raises the chamber pressure to ~3.5·10-3 torr.

A nice advantage of a tunable probe wavelength is the ability to use optical resonances of the transducer to amplify signal amplitude. To test how optical resonances can enhance thermoreflectance signal, we performed wavelength dependent TDTR measurements on a 60 nm Au film. The d-bands in Au are ~2.5 eV below the Fermi level. In Fig. 1.3, we show TDTR measurements with pump and probe energies of 1.58 and 2.61 eV, where at 2.61eV the thermoreflectance signal is maximized. A probe energy of 2.61 eV results in a thermoreflectance signal ~4x larger than at 1.58 eV. The 2.61 eV probe results in Fig. 1.3 are scaled to account for decreased absorption of the pump energy at 1.58 eV, and the reduced modulation amplitude of our EOM at 1.58 vs. 2.61 eV. Both data sets are in good agreement with heat-diffusion equation predictions with a sapphire thermal conductivity of $\Lambda \approx 38$ W m^{-1} K^{-1} and an Au/sapphire interface conductance of $G \approx 50$ MW m^{-2} K^{-1}.

Interestingly, while the shape of the TDTR signal for probe wavelengths at both 1.58 and 2.61 eV are nearly identical at delay times longer than 10 ps, the shape of the curves differ significantly at picosecond time-delays. We credit this difference to increased sensitivity of the thermoreflectance to the electron temperature distribution because the electrons are hundreds of Kelvin hotter than the phonons for 1-2 picoseconds after pump excitation. Prior studies have

suggested that the thermoreflectance of noble metals is primarily sensitive to the electron temperature near interband transitions [19, 20].

To explore the effect of the Au interband transitions on the MOKE signal from Au/Co multilayers, we performed a series of TR-MOKE with varied probe wavelengths. In Fig.1.4 we show the results from TR-MOKE scans with pump and probe energies of 1.58 and 2.36 eV. We chose 2.36 eV probe for comparison to our 1.58 eV data because the signal was a maximum at 2.36 eV. After accounting for differences in absorption and EOM modulation amplitude, we observe that the MOKE signal from Au/Co increases by ~2x at 2.36 vs. 1.58 eV.

IV. Summary. — We have presented the instrumentation for a high sensitivity pump/probe system whose pump and probe wavelengths are broadly tunable. The system uses takes advantage of both the wavelength tunability, and ultra-low-noise of Ti:sapphire oscillators to sensitively detect changes in temperature, magnetic moment, and strain in optically excited samples. We have analyzed the effect of optical elements with broad band dielectric coatings on our MOKE experiments. Finally, we have shown the utility of tuning the probe energy to coincide with interband transitions of the metal for increasing thermoreflectance, magneto-optic, and picosecond-acoustic signals.
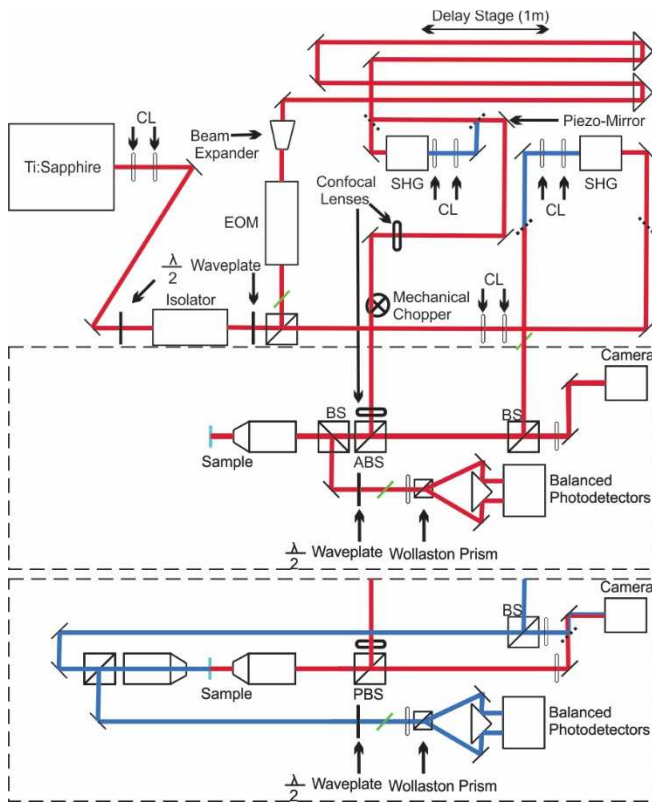
Figure 1.1 Ti:Sapphire laser and pump-probe laser system. A tunable Ti:Sapphire laser (690-1050nm, 345-530nm) with a repetition rate of 80MHz and pulse duration of 700fs is modulated with an Electro-Optic-Modulator, and mechanical chopper. A radio-frequency lock-in (SRS 844) and computer-based audio frequency lock-in amplifier (NI-DAQ PCI-4474) are used to detect pump induced changes in reflection and polarization.
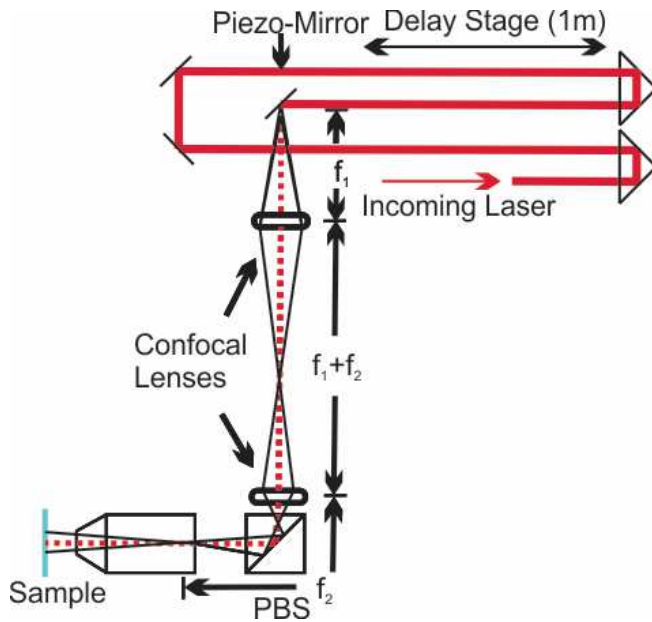
Figure 1.2 Confocal pump lens configuration. After the pump beam exits the delay stage mirrors, a mirror mounted with x and y piezo electric motors is used to adjust the position of the pump beam on the sample. Two lenses whose separation length depends on the respective focal lengths are used to provide a consistent entry point into the objective lens, while also allowing for x and y displacement on the sample surface. This consistent entry point into the objective while retaining movement of the beam on the sample surfaces removes aberrations due changes in entry positions, as well as beam-offset measurements for characterizing the beam spot size.
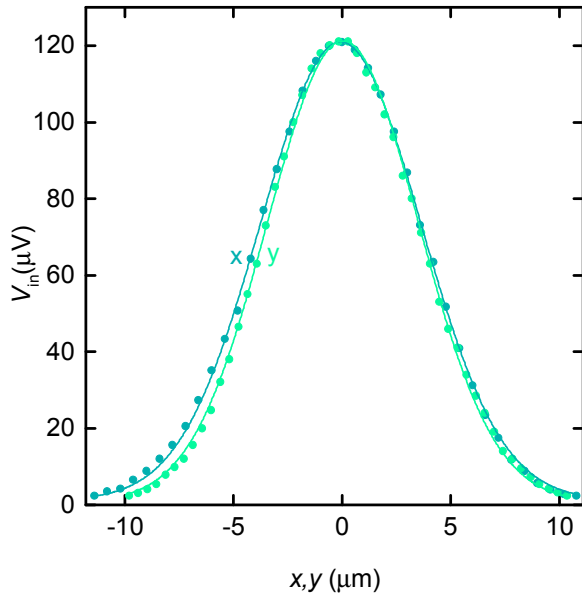
Figure 1.2b. Beam offset measurements with Gaussian fits in the x and y directions. By using a mirror mounted with x and y piezo-electric motors the spot size of the pump and probe overlap was determined on micron length scales. Calibration of the rad/step of the piezo-electric motors was conducted using a beam profiler and by knowing the focal length of the objective lens used, the $\frac{1}{e^2}$ beam radius was experimentally measured for the x and y direction.
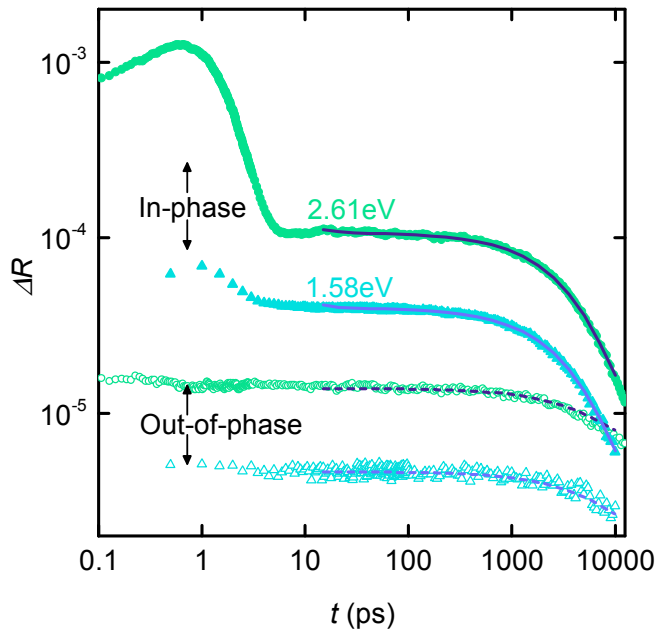
Figure 1.3. Thermoreflectance measurements and model predictions of 60nmAu on sapphire. In phase (green cirlces) and out of phase (blue triangles) thermoreflectance data and model predictions were conducted as a function of probe energy (1.58eV and 2.61eV). Change in reflectance and model predictions indicate that our system is in agreement with previous Au thermoreflectance measurements.
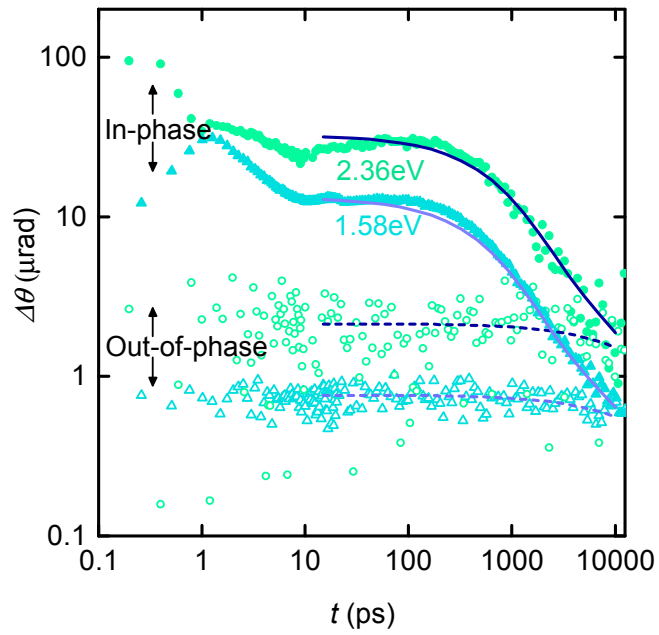
Figure 1.4. TR-MOKE measurements as of a 5nm/AuCoML/sapphire sample as a function of probe energy (1.58eV 2.36eV). In phase (green circles) and out of phase (blue triangles) experimental results and model predictions show a change in Kerr angle after ultra-fast laser heating.

References

1. Cahill, D.G., *Analysis of heat flow in layered structures for time-domain thermoreflectance.* Review of Scientific Instruments, 2004. **75**(12): p. 5119-5122.

2. Wilson, R., B.A. Apgar, L.W. Martin, and D.G. Cahill, *Thermoreflectance of metal transducers for optical pump-probe studies of thermal properties.* Optics express, 2012. **20**(27): p. 28829-28838.

3. Hohensee, G.T., W.-P. Hsieh, M.D. Losego, and D.G. Cahill, *Interpreting picosecond acoustics in the case of low interface stiffness.* Review of Scientific Instruments, 2012. **83**(11): p. 114902.

4. Yang, Y., R.B. Wilson, J. Gorchon, C.-H. Lambert, S. Salahuddin, and J. Bokor, *Ultrafast magnetization reversal by picosecond electrical pulses.* Science Advances, 2017. **3**(11).

5. Rost, C.M., J. Braun, K. Ferri, L. Backman, A. Giri, E.J. Opila, J.-P. Maria, and P.E. Hopkins, *Hafnium nitride films for thermoreflectance transducers at high temperatures: Potential based on heating from laser absorption.* Applied Physics Letters, 2017. **111**(15): p. 151902.

6. Jiang, P., X. Qian, and R. Yang, *A new elliptical-beam method based on time-domain thermoreflectance (TDTR) to measure the in-plane anisotropic thermal conductivity and its comparison with the beam-offset method.* arXiv preprint arXiv:1803.06551, 2018.

7. Li, M., J.S. Kang, and Y. Hu, *Anisotropic thermal conductivity measurement using a new Asymmetric-Beam Time-Domain Thermoreflectance (AB-TDTR) method.* Review of Scientific Instruments, 2018. **89**(8): p. 084901.

8. Sun, B. and Y.K. Koh, *Understanding and eliminating artifact signals from diffusely scattered pump beam in measurements of rough samples by time-domain thermoreflectance (TDTR).* Review of Scientific Instruments, 2016. **87**(6): p. 064901.

9. Chen, J.-Y., J. Zhu, D. Zhang, D.M. Lattery, M. Li, J.-P. Wang, and X. Wang, *Time-resolved magneto-optical Kerr effect of magnetic thin films for ultrafast thermal characterization.* The journal of physical chemistry letters, 2016. **7**(13): p. 2328-2332.

10. Kang, K., Y.K. Koh, C. Chiritescu, X. Zheng, and D.G. Cahill, *Two-tint pump-probe measurements using a femtosecond laser oscillator and sharp-edged optical filters.* Review of Scientific Instruments, 2008. **79**(11): p. 114901.

11. Heilpern, T., M. Manjare, A.O. Govorov, G.P. Wiederrecht, S.K. Gray, and H. Harutyunyan, *Determination of hot carrier energy distributions from inversion of ultrafast pump-probe reflectivity measurements.* Nature communications, 2018. **9**(1): p. 1853.

12. Khorsand, A.R., M. Savoini, A. Kirilyuk, A.V. Kimel, A. Tsukamoto, A. Itoh, and T. Rasing, *Element-Specific Probing of Ultrafast Spin Dynamics in Multisublattice Magnets with Visible Light.* Physical Review Letters, 2013. **110**(10): p. 107205.

13.   Visnovsky, S., M. Nyvlt, V. Prosser, J. Ferré, G. Pénissard, D. Renard, and G. Sczigel, *Magneto-optical effects in Au/Co/Au ultrathin film sandwiches.* Journal of magnetism and magnetic materials, 1993. **128**(1-2): p. 179-189.

14.   Jakubisova-Liskova, E., S. Visnovsky, H. Chang, and M. Wu, *Optical spectroscopy of sputtered nanometer-thick yttrium iron garnet films.* Journal of Applied Physics, 2015. **117**(17): p. 17B702.

15.   Tas, G. and H.J. Maris, *Electron diffusion in metals studied by picosecond ultrasonics.* Physical Review B, 1994. **49**(21): p. 15046.

16.   Devos, A. and A. Le Louarn, *Strong effect of interband transitions in the picosecond ultrasonics response of metallic thin films.* Physical Review B, 2003. **68**(4): p. 045405.

17.   Hamrle, J., J. Ferré, M. Nývlt, and Š. Višňovský, *In-depth resolution of the magneto-optical Kerr effect in ferromagnetic multilayers.* Physical Review B, 2002. **66**(22): p. 224423.

18.   Schellekens, A.J., N. de Vries, J. Lucassen, and B. Koopmans, *Exploring laser-induced interlayer spin transfer by an all-optical method.* Physical Review B, 2014. **90**(10): p. 104429.

19.   Hohlfeld, J., D. Grosenick, U. Conrad, and E. Matthias, *Femtosecond time-resolved reflection second-harmonic generation on polycrystalline copper.* Applied Physics A, 1995. **60**(2): p. 137-142.

20.   Hohlfeld, J., S.-S. Wellershoff, J. Güdde, U. Conrad, V. Jähnke, and E. Matthias, *Electron and lattice dynamics following optical excitation of metals.* Chemical Physics, 2000. **251**(1-3): p. 237-258.

CHAPTER 2

Spin-Dependent Seebeck Effect

Ultrafast Measurements of the Longitudinal Spin Seebeck Effect in Nanoscale
Metal-Iron Garnet Bilayers

We investigate picosecond spin-currents across Au/iron-garnet interfaces in response to ultrafast laser heating of the electrons in the Au film. In the picoseconds after optical heating, large interfacial spin currents occur due to an interfacial temperature imbalance between electrons in the metal and magnons in the insulator. We use time-resolved magneto-optic Kerr effect (TR-MOKE) and time domain thermoreflectance (TDTR) measurements to measure the magnitude of the spin-current due to interfacial temperature gradients between Au and $X_3Fe_5O_{12}$, where X is Tm, Y, Eu, Tb. We observe a spin-current between Au/TmIG that is three times larger than Au/YIG. The factor of three difference is comparable to changes we observe by changing the interface quality of Au/TbIG and Au/EuIG layer via different sample preparations.

I. Introduction. — The longitudinal spin Seebeck effect (LSSE) describes the injection of spin currents into a nonmagnetic metal because of a temperature gradient across a nonmagnetic-metal/magnetic-insulator heterostructure [1]. Understanding spin currents emanating from magnetic insulators is of fundamental interest to the magnetic community. The SSE may have applications for spintronic information technologies and heat waste scavenging [2].

Spin current across the metal/insulator interface relies on magnon emission and absorption at the interface by flipping the spin of an itinerant electron in the metal [2]. A temperature difference across the interface between electrons and magnons creates an imbalance in the number of magnons emitted vs. absorbed. The resulting heat-current is often approximated as

$$j_Q = G_{e-m}\Delta T_{e-m} \ , \qquad (1)$$

where G_{e-m} is the electron-magnon interfacial thermal conductance and ΔT_{e-m} is the temperature drop across the interface between electrons and magnons. Since this heat-current is due to the absorption/emission of magnons, it is accompanied by a spin-current. The spin current is hypothesized to equal the product of the heat-current and the ratio of angular momentum per unit of thermal energy,

$$j_s = j_Q \left(2e / k_B T\right). \qquad (2)$$

Spin injection across the interface is of central importance to the SSE [2]. However, relatively little data exists regarding the magnitude of G_{e-m} and how it depends on microscopic properties of the metal and magnetic-insulator. The reason for this is that , typically, the LSSE is not measured directly, but rather inferred from a transvers electrical current measurement via the inverse spin Hall effect (ISHE)[3]. The LSSE is a complex phenomenon and depends on the electron-phonon coupling in the metal layer, the electron-magnon coupling at the metal-magnetic insulator interface, and the magnon-phonon coupling in the magnetic insulator. If the spin Hall effect is used to

determine the LSSE, the spin Hall angle of the metal must also be known. Ideally when a phenomenon is so complex, each of the dependent variables would be measured with independent experiments. Furthermore, systematic effects in transverse thermopower measurements introduce reproducibility problems. A recent round robin measurement of the same device by five research groups resulted in values of S that varied by a factor of ten [4].

Here, we follow Ref. [5] and use a combination of time-resolved magneto optic Kerr effect (TR-MOKE) and time-domain thermo-reflectance (TDTR) measurements to quantify G_{e-m} in Au/iron-garnet insulator bilayers. TDTR is a well-established method for measuring thermal transport properties and characterizing temperature fields due to laser heating [6]. TR-MOKE measurements allow us to directly measure spin accumulation in the non-magnetic layer. In TDTR and TR-MOKE experiments, an ultrafast pump laser heats electron in a non-magnetic layer. A time-delayed probe pulse monitors the temperature evolution via changes in reflectance. Spin accumulation in the metal that results from electron-magnon scattering is detected via changes in the polarization of the reflected probe laser (MOKE).

We characterize the LSSE in nanoscale systems comprised of a non-magnetic metal (Au) and an iron garnet magnetic insulator ($X_3Fe_5O_{12}$, X:Tm, Y, Eu, Tb) layer. For Tm, Eu, and Tb, the rare-earth ion replaces Y^{3+} ion. The magnetic moment of the rare-earth is antiparallel to the tetrahedral Fe ions, parallel to the octahedral ions. As a result, moving from Y to Tm to Eu to Tb systematically decreases the total magnetization of the iron-garnet.

II. Sample preparation. —The iron garnets were grown via laser ablation deposition in a high vacuum environment. The iron-garnet samples were deposited on single crystal Gallium Gadolinium Garnet $Gd_3Ga_5O_{12}$ (GGG) or Neodynium doped Gallium Gadolinium Garnet Nd: $Gd_3Ga_5O_{12}$ (NGGG) substrates. The magnetic insulator layers are ~20nm thick. The magnetic insulator samples then went through a rapid thermal annealing procedure in a cleanroom

29

environment. The samples were then loaded into a high vacuum sputtering chamber (AJA Orion) to deposit the Au film. Prior to Au film deposition, the samples were annealed at 200 C for 1 hr in in a mixture of UHP Oxygen and Argon. After the iron garnet samples cooled in high vacuum to room temperature, Au was sputtered via DC magnetron sputtering at 3.5 mTorr at a power of 10 W. The target sample distance was ~10cm. The majority of the Au layers sputtered were ~60nm thick. We also performed measurements on samples with 5 nm and 40 nm Au films and prepared one 20nmPt/TmIG/NGGG sample, though little to no signal was present due to the high spin-flip behavior of Pt. Film thicknesses were characterized via a combination of probe beam deflection measurements, and/or TDTR measurements on films sputtered reference substrates with known thermal properties, e.g. sapphire or BK7 glass.

To understand the importance of interface quality, we also varied how the garnet-sample surface was cleaned prior to the deposition of the Au film. Different interface preparation methods were used, e.g. solvent cleaning, plasma cleaning, chemical etching, annealing, etc. A more in-depth discussion of how interface quality effects our results is in section *V*.

III. Experimental methods. — Our pump-probe laser system detects changes in reflectance (TDTR) and polarization of reflected light (TR-MOKE) to monitor pump induced changes in temperature and magnetic moment of the non-magnetic film. Our pump-probe system uses a variable wavelength (690-1060nm) Ti:sapphire laser with a repetition rate of 80MHz and pulse width of 700 femto seconds. An electro-optic modulator (EOM) modulates the pump laser at a frequency of 10.7MHz where the laser intensity noise of Ti:sapphire oscillator is shot-noise limited. A delay stage varies the arrival time of the pump laser pulses to the sample relative to the probe pulses. For TDTR measurements and probe beam deflection measurements, the reflected probe laser is focused on a single photo-diode to monitor pump-induced changes in reflectance. For TR-MOKE measurements, the reflected probe beam is split into orthogonal polarizations and focused

30

onto one of two photodiodes in a balanced photodetector. The RF signal from the photo detector was is measured with a RF lock-in (SRS 844) and computer lock in (NI-DAQ PCI-4474).

IV. Results. — Time-domain thermoreflectance results. We fit the TDTR data on time-scales shorter than 10 ps with a two-temperature model. The only fit parameter was the electron-phonon coupling constant. The two-temperature model is in good agreement with our data with $g_{ep} \approx 2 \cdot 10^{16}$ W m^{-3} K^{-1}, see Fig. 2.1. After 10 picoseconds, the electrons and phonons in the Au layer are in thermal equilibrium and a two-temperature model is not necessary. We fit the long-time delay data with a multilayered solution to the heat-diffusion equation [6]. We include further discussion of TDTR below as a method for probing interfacial quality.

To investigate electron-phonon coupling in the Au, we needed to understand the temperature evolution of the electrons and the phonons, respectively, in the Au layer. We accomplished this by conducting wavelength dependent TDTR measurements of a 60 nm Au layer, as shown in chapter 3 of this work. Wavelength dependent TDTR measurements are advantageous for our first area of interest due to the electron distribution of Au [8]. Hohlfeld *et al.* showed that the thermoreflectance of Au for photon energies near 2.5 eV possess more sensitivity to electron temperature than photon energies in the near-infrared, e.g. 1 eV. Wilson *et al.* report that in the infrared, the experimental values for Au thermoreflectance are consistent with simple models that assume the thermoreflectance in the near-infrared is dominated by the phonon temperature. At lower energies the s/p electrons in the Au are the predominant oscillators responsible for the reflection of the incident probe light, while increasing energies allows for transitions from electrons in the d bands to partake in the probe light reflection. We assume the thermoreflectance is a combination of the change in electron and phonon temperature,

$$\Delta R = \alpha \Delta T_e + \beta \Delta T_{ph},\qquad(3)$$

where α and β are sensitivity scalars for the electron and phonon contribution for the thermoreflectance that depend on wavelength. Thus, by varying the probe energy incident on the Au layer, we vary our sensitivity to the electron and phonon temperature response, which gives us vital information regarding the electron-phonon coupling in the Au layer.

We perform TR-MOKE measurements to measure the magnitude of spin accumulation in the 60nm Au film following laser heating. The amount of spin-accumulation in the Au following laser heating depends on the Au thickness, the spin-flip scattering time of Au electrons, the electron-magnon interface conductance G_{e-m}, and the magnitude of the temperature difference between the Au electrons and iron-garnet magnons. The only uknown is G_{e-m}, therefore we can deduce G_{e-m} from TR-MOKE measurements of spin-accumulation.

We use polar MOKE to detect spin-accumulation in the Au with a probe beam energy of 1.58 eV. The polarization of the spin-current is determined by the orientation of the iron-garnet magnetic moment. Therefore, our experiment requires the magnetic moment of the iron-garnet point in the out-of-plane direction. We control the orientation of the iron-garnet field with an 0.3T external magnetic field from a nearby NdFeB permanent magnet. Each measurement consists of two scans with the external magnetic field in opposite directions. The final MOKE signal we report is the difference in signal measured with positive vs. negative magnetic field.

We show the results of TR-MOKE measurements of four iron-garnet samples in Fig.2.2. After the pump laser irradiates the Au at a time delay of 0 ps, spin starts to accumulate in the Au film. The peak in accumulation occurs at the end of the pump laser pulse duration. After the pump laser is no longer present, the hot electrons cool, the spin accumulation dissipates due to spin-flip scattering, and the signal decays towards zero.

The data in Fig. 2.2 is normalized for pump fluence. Therefore, the differences in signal heights are a result of differences in G_{e-m} between the Au and various iron-garnets. The value of G_{e-m} for TmIG is a factor of 3 higher than YIG. We see no correlation in the strength of signal and the magnetic moment of the iron-garnet. Yttrium-iron-garnet has the highest magnetic moment, but weakest signal. The Au/TmIG sample produces higher spin-accumulation signals than the Au/TbIG sample, despite Tb moment being larger. We conclude other effects, e.g. interfacial structure or iron-garnet stoichiometry govern the signal strength. Further characterization of the iron garnets would be helpful in corroborating or dismissing this.

To test how interface properties effect G_{e-m}, we performed several experiments to study interfacial quality. We performed TDTR measurements of the total thermal resistance arising from the metal/garnet-insulator interface, the garnet-film, and the garnet-film/substrate interface. We also performed probe beam deflection measurements of the lifetime of acoustic waves in the Au film, which depends on interface quality.

TDTR is a sensitive probe of interfacial properties because the time-evolution of the temperature of the Au film is primarily determined by the phonon interface conductance of the Au/iron-garnet layer. The time-evolution is also governed by the thermal conductivity of the iron-garnet layer, and the thermal effusivity of the substrate. TDTR measurements of the temperature evolution of the Au surface of a 60 nm Au/TmIG/NGGG sample are shown in Fig. 2.3. This data is representative of similar scans we conducted on all samples. To analyze the TDTR data, we fixed the thermal conductivity of the iron-garnet layer to 5 W m^{-1} K^{-1}, and the substrate effusivity to literature values. We treat the interface conductance between the metal film and iron-garnet layer as a fit parameter in our model.

Table 1.1 summarizes the interfacial conductivities for all samples we performed TR-MOKE samples on. The samples labeled in table 1.1 were prepared in a variety of ways, specifically regarding their individual surface treatment before DC magnetron sputtering of the Au film.

TmIG1a was deposited onto NGGG followed by rapid thermal annealing in oxygen. The sample was taken immediately from the rapid thermal anneal chamber and placed into our AJA Orion sputter chamber. Once in the sputter chamber, the sample was annealed to 200C for 1 hour in a gas mixture of 10mTorr Argon and 1mTorr UHP Oxygen. The sample was allowed to cool to room 28C and then Au was sputtered onto the TmIG1a.

TmIG1a was then submerged in an Au etchant (Sigma Aldrich Standard Gold Etchant) for 10 minutes followed by Piranha etching for 1 hour. TmIG1a was then immediately placed into our AJA Orion sputter chamber and was subsequently annealed to 200C for 1 hour in a gas mixture of 10mTorr argon and 1mTorr UHP oxygen. The sample was allowed to cool to room 28C and then Au was sputtered onto the TmIG1a, now to be called TmIG1b.

YIG1 and was deposited onto GGG followed by rapid thermal annealing in oxygen. The sample was taken immediately from the rapid thermal anneal chamber and placed into our AJA Orion sputter chamber. Once in the sputter chamber, the sample was annealed to 200C for 1 hour in a gas mixture of 10mTorr argon and 1mTorr UHP oxygen. The sample was allowed to cool to room 28C and then Au was sputtered onto the YIG1. YIG2 followed a similar process as YIG1 with the only difference being the thickness of Au sputtered.

TbIG1a was deposited onto GGG followed by rapid thermal annealing in oxygen. The sample was not taken immediately from the rapid thermal anneal chamber, but rather left in ambient conditions for several weeks. TbIG1a was then Piranha etched for 1 hour and then immediately placed into our AJA Orion sputter chamber. Once in the sputter chamber, the sample was annealed

to 200C for 1 hour in a gas mixture of 10mTorr Argon and 1mTorr UHP Oxygen. The sample was allowed to cool to room 28C and then Au was sputtered onto TbIG1a.

TbIG1a was then submerged in an Au etchant (Sigma Aldrich Standard Gold Etchant) for 2 minutes followed by submersion in acetone for 1 hour and then ethanol for 15 minutes. TbIG1a was then immediately placed into our AJA Orion sputter chamber and was subsequently annealed to 200C for 1 hour in a gas mixture of 10mTorr argon and 1mTorr UHP oxygen. The sample was allowed to cool to room 28C and then Au was sputtered onto the TbIG1a, now to be called TbIG1b.

TbIG1b was then submerged in an Au etchant (Sigma Aldrich Standard Gold Etchant) for 2 minutes followed by Piranha etch for 1 hour. TbIG1b was then immediately placed into our AJA Orion sputter chamber and was subsequently annealed to 200C for 1 hour in a gas mixture of 10mTorr argon and 1mTorr UHP oxygen. The sample was allowed to cool to room 28C and then Au was sputtered onto the TbIG1b, now to be called TbIG1c.

TbIG2a was deposited onto GGG followed by rapid thermal annealing in oxygen. The sample was taken immediately from the rapid thermal anneal chamber and placed into our AJA Orion sputter chamber. Once in the sputter chamber, the sample was annealed to 200C for 1 hour in a gas mixture of 10mTorr Argon and 1mTorr UHP Oxygen. The sample was allowed to cool to room 28C and then Au was sputtered onto the TbIG2a.

TbIG2a was then submerged in an Au etchant (Sigma Aldrich Standard Gold Etchant) for 2 minutes followed by Piranha etch for 1 hour. TbIG2b was then immediately placed into our AJA Orion sputter chamber and was subsequently annealed to 200C for 1 hour in a gas mixture of 10mTorr argon and 1mTorr UHP oxygen. The sample was allowed to cool to room 28C and then Au was sputtered onto the TbIG2a, now to be called TbIG2b.

EuIG1 was deposited onto GGG followed by rapid thermal annealing in oxygen. The sample was not taken immediately from the rapid thermal anneal chamber, but rather left in ambient

conditions for several weeks. EuIG1 was submerged in acetone for 1 hour followed by 15 minutes in ethanol. EuIG1 was then immediately placed into our AJA Orion sputter chamber. Once in the sputter chamber, the sample was annealed to 200C for 1 hour in a gas mixture of 10mTorr Argon and 1mTorr UHP Oxygen. The sample was allowed to cool to room 28C and then Au was sputtered onto EuIG1.

EuIG2 was deposited onto GGG followed by rapid thermal annealing in oxygen. The sample was taken immediately from the rapid thermal anneal chamber and placed into our AJA Orion sputter chamber. Once in the sputter chamber, the sample was annealed to 200C for 1 hour in a gas mixture of 10mTorr Argon and 1mTorr UHP Oxygen. The sample was allowed to cool to room 28C and then Au was sputtered onto the EuIG2.

EuIG3 was deposited onto GGG followed by rapid thermal annealing in oxygen. The sample was not taken immediately from the rapid thermal anneal chamber, but rather left in ambient conditions for several weeks. EuIG3 was Piranha etched for 1 hour. EuIG3 was then immediately placed into our AJA Orion sputter chamber. Once in the sputter chamber, the sample was annealed to 200C for 1 hour in a gas mixture of 10mTorr Argon and 1mTorr UHP Oxygen. The sample was allowed to cool to room 28C and then Au was sputtered onto EuIG3. EuIG4 followed the same process as EuIG3.

EuIG5 was deposited onto GGG followed by rapid thermal annealing in oxygen. The sample was not taken immediately from the rapid thermal anneal chamber, but rather left in ambient conditions for several weeks. EuIG5 was submerged in acetone for 1 hour followed by 15 minutes in ethanol. EuIG1 was then immediately placed into our AJA Orion sputter chamber. Once in the sputter chamber, the sample was annealed to 200C for 1 hour in a gas mixture of 10mTorr Argon and 1mTorr UHP Oxygen. The sample was allowed to cool to room 28C and then Au was sputtered onto EuIG5.

Interfacial thermal conductance is sensitive to interfacial atomic bonding strength, interfacial roughness and disorder [7]. The interface conductances of the samples in Fig. 2.2 showing high interfacial thermal conductivities on the order of 0.1 W m^{-1} K^{-1}. Since the phonon interfacial thermal conductance does not vary appreciably between these samples, we can assume that the adhesion between the metal and iron-garnet films, the interfacial roughness, and interfacial disorder are not appreciably different between samples.

As a further test of interface quality, we used time-domain probe-beam deflection as an additional probe of interfacial quality [9]. The time-scale that the acoustic oscillations persist over provides another measure of interfacial quality. We show typical results for the probe-beam-deflection experiments in Fig. 2.4.

We find that treatments of the iron-garnet surface have a significant effect on the magnitude of the interfacial spin Seebeck effect, i.e the amount of spin-accumulation we observe for a fixed amount of pump fluence. In Fig. 2.5, we show three separate TR-MOKE measurements of the same TbIG film. For the first measurement, we piranha cleaned the TbIG before loading in the Au sputter The initial 60nmAu layer was etched using a chemical Au etchant and the Tb sample was then cleaned with acetone and ethanol and the sample preparation procedures from section II were carried out, although with a slightly thinner Au thickness of 40nm due to changes in sputter rate. TR-MOKE measurements were conducted and the Au film was etched away again, though on this occasion the surface was cleaned with a 1 hour soak in Piranha solution. As can be seen from Table 2.1 and from Fig. 2.5, the signal decreased dramatically after treating the surface with acetone and ethanol and the signal was then able to be partially restored to its original value after cleaning with Piranha. This corroborates the importance of a pristine surface in these SSE measurements.

To measure the thickness of the Au layer, beam deflection measurements were carried out on several samples, in which the period of oscillation in the TDTR signal is related to the thickness of

Au via the longitudinal speed of sound in Au, as shown in Fig. 2.4. Table 2.2 shows the period of oscillation, as well as the damping coefficient, in which the dampened harmonic equation similar to [5] was used.

V. Summary.— By using a medley of pump-probe experiments, we were able to gain experimental results pertaining to the dependent variables of the LSSE in Au/IG bilayer systems on sub-picosecond timescales. Typically the SSE is measured via secondary effects, such as the inverse spin Hall effect (ISHE), and a charge current is then related to a spin current. Ideally the SSE would be investigated directly, and described fully. By using a series of TDTR and TR-MOKE measurements I was able to describe the spin accumulation in Au/iron garnet layers as a function of wavelength and various iron garnet spin sources. We are able to experimentally determine the electron-phonon coupling a $2 \cdot 10^{16} W/m^3 K \, a$ in order to understand the temperature evolution throughout the Au film We also obtain SSE coefficient of $1 \cdot 10^8 A/m^2 K$ for AuTmIG1a which is in good agreement with other works.
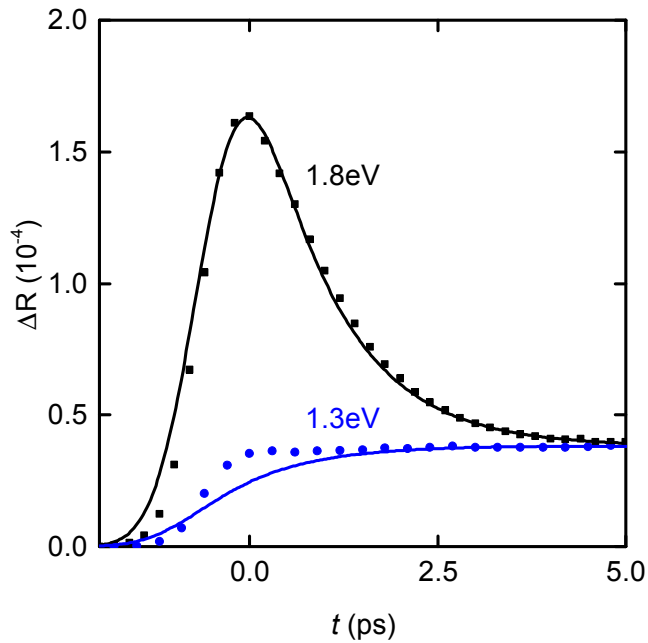
FIG. 2.1 Thermoreflectance data and model predictions of 60nmAu/Sapphire. TDTR measurements were performed on the Au layer of a 60nmAu/Sapphire as a function of probe energy (1.3 and 1.8eV). Thermoreflectance data with model prediction (black squares and line) at 1.8eV provide information regarding the temperature of electrons in the Au. Data and model prediction (blue circle and line) at 1.3eV provide information regarding the temperature of phonons on the Au.
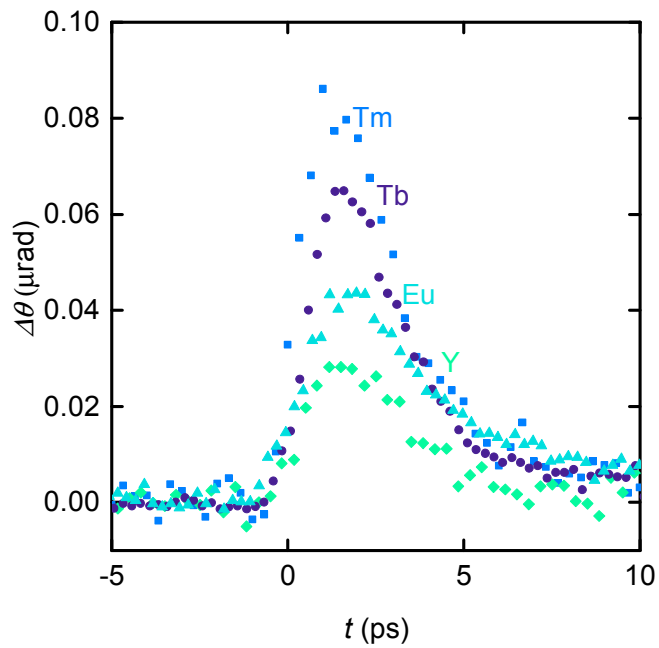
Figure 2.2. TR-MOKE of 60nmAu as a function of iron garnet spin source. 60nmAu sputtered onto thulium (blue squares), terbium (purple circles), europium (light blue triangles), and yttrium (green diamonds). The amount of spin accumulation after femto-second laser absorption in the Au layer depends strongly on the type of-iron garnet.
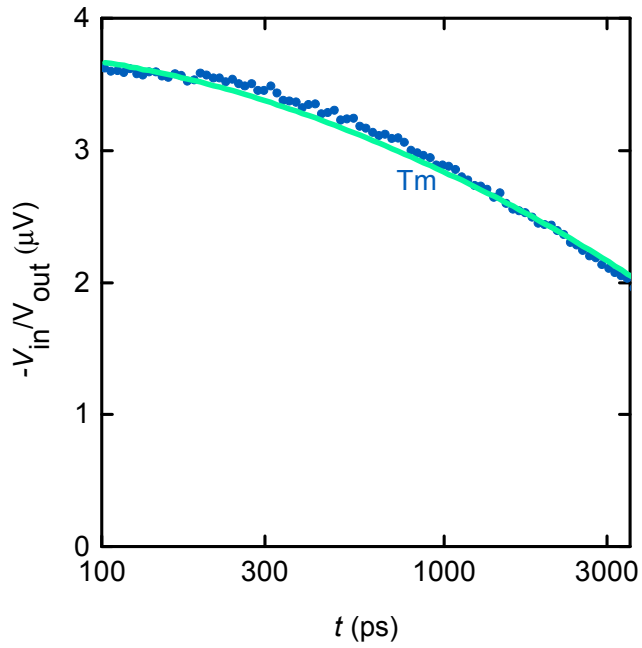
FIG.2.3 Thermoreflectance data and model prediction. A TDTR measurement was performed on 60nmAu/TmIG/NGGG sample at 1.58eV probe energy. The experimental ratio of the in-phase and out-of-phase data (navy blue circles) were fit with a thermal model (green line) in order to obtain the interfacial thermal conductivity ($0.107\frac{W}{mK}$). The interface quality effects spin injection into the Au. Similar experiments and modeling were performed an all our bilayer systems.
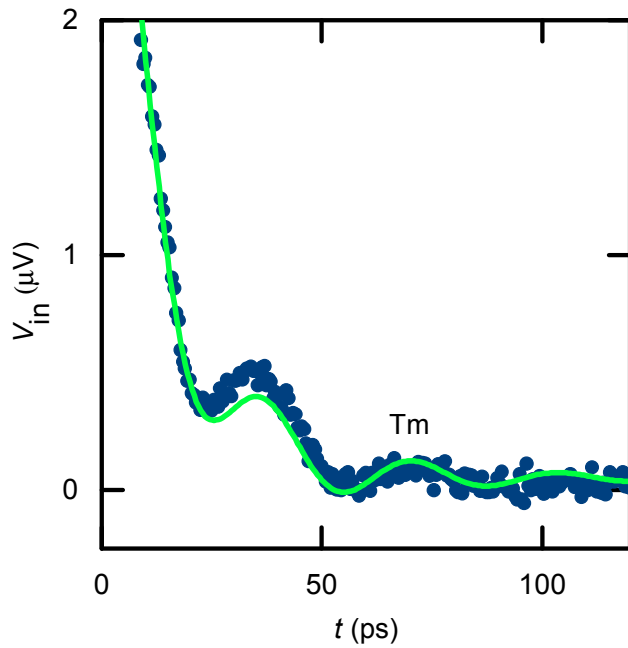
FIG.2.4 Beam deflection data and model prediction. A beam deflection TDTR measurement was performed on the Au layer of a 60nmAu/TmIG/NGGG sample. Periodic oscillations in the experimental data (navy blue circles) pertain to the thickness of the Au layer via dampened harmonic oscillation. Our experimental data was fit with a least squares model prediction (green line) governed by dampened harmonic oscillation. Similar experiments and modeling were
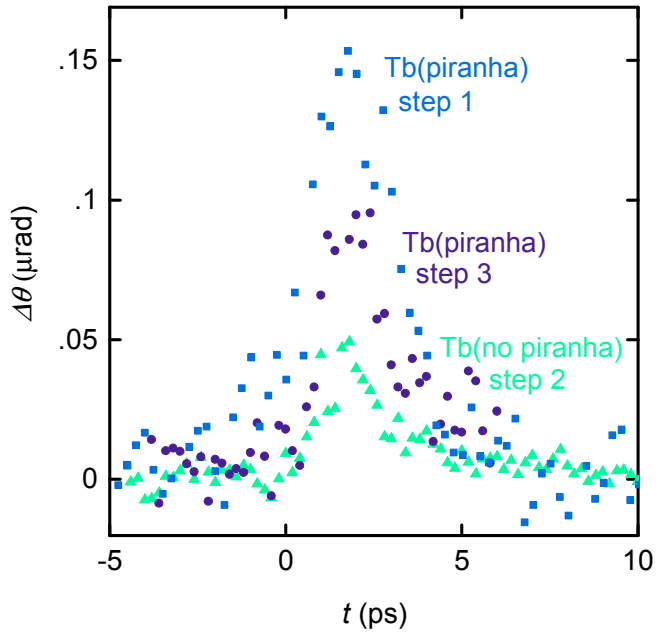
FIG. 2.5 TR-MOKE data of Au on TbIG. The 60nm Au was chemically etched away from the Au/TbIG sample. Following the Au etch, the sample was cleaned with acetone and ethanol and approx. 40nm was sputtered onto the TbIG (due to changes in sputter rate). A thinner Au layer should increase the temperature gradient between Au and TbIG because the electron temperature will be higher for the same absorbed fluence. However, the TR-MOKE signal decreased dramatically. We credit the decrease to poor interface quality. After etching the Au layer once more, Piranha solution was used to clean the surface and the signal then was able to somewhat recover in strength suggesting that the acetone and ethanol cleaning method severely hindered the spin injection into the Au layer.

Sample	Au (nm)	Λ (W/m•K)
TmIG1a	62.5	.107
TmIG1b	41.5	.095
YIG1	61.5	.103
YIG2	45.5	.086
TbIG1a	59.8	.099
TbIG1b	42.5	.081
TbIG1c	38.3	.094
TbIG2a	61.3	.091
TbIG2b	40.5	.100
EuIG1	67	.070
EuIG2	60	.072
EuIG3	55.5	.110
EuIG4	63	.080
EuIG5	58	.077

Table. 2.1 Thermal conductivity fits for Au/IG samples. TDTR measurements were fit using a thermal model and with the Au, iron-garnet, and substrate material properties known, the interface was used as the fitting parameter. The interfacial conductivity changed depending on sample treatment, as discussed above.

Sample	Au (nm)	Γ (GHz	T_a(ps)	δ
TmIG	60	30.3	33.0	1.0
YIG	60	38.9	30.4	1.6
TbIG	60	36.4	28.9	2.0
EuIG	60	34.1	29.2	1.7
EuIG	60	33.3	30.9	1.6
YIG	43	42.6	20.6	2.0

Table. 2.2 Beam deflection table containing period of oscillation, the corresponding thickness of Au, and the dampening coefficient. TDTR/beam deflection measurements were carried out several Au/IG samples and were then fit with a dampened harmonic function as shown in Fig 2.4.

References

1.   Xiao, J., et al. (2010). "Theory of magnon-driven spin Seebeck effect." Physical Review B 81(21): 214418.

2.   Uchida, K., et al. (2014). "Longitudinal spin Seebeck effect: from fundamentals to applications." Journal of Physics: Condensed Matter 26(34): 343202.

3.   Uchida, K., et al. (2008). "Observation of the spin Seebeck effect." Nature 455(7214): 778.

4.   Sola, A., et al. (2018). "Spincaloritronic measurements: a round robin comparison of the longitudinal spin Seebeck effect." IEEE Transactions on Instrumentation and Measurement.

5.   Kimling, J., et al. (2017). "Picosecond spin Seebeck effect." Physical review letters 118(5): 057201.

6.   Cahill, D.G., Analysis of heat flow in layered structures for time-domain thermoreflectance. Review of Scientific Instruments, 2004. 75(12): p. 5119-5122
7.   Shen, M., et al. (2011). "Bonding and pressure-tunable interfacial thermal conductance." Physical Review B 84(19): 195432.

8.   Hohlfeld, J., S.-S. Wellershoff, J. Güdde, U. Conrad, V. Jähnke, and E. Matthias, Electron and lattice dynamics following optical excitation of metals. Chemical Physics, 2000. 251(1-3): p. 237-258

9.   Hohensee, G.T., W.-P. Hsieh, M.D. Losego, and D.G. Cahill, *Interpreting picosecond acoustics in the case of low interface stiffness.* Review of Scientific Instruments, 2012. **83**(11): p. 114902

CHAPTER 3
Thermoreflectance of Au

Electron and Phonon Contribution to Thermoreflectance in Au as a function of Probe Energy

In the femto- to pico-seconds after laser excitation of a metal, electrons and phonons are not in thermal equilibrium. Conventional optical and electrical thermometry techniques assume local thermal equilibrium exists in the material, i.e. that electrons and phonons are the same temperature. In this study we revaluate this assumption for thermoreflectance experiments, a common type of optical thermometry. We use wavelength dependent time domain thermoreflectance (TDTR) to study whether electron and phonon temperatures can be determined independently of one another. We show that the sensitivity of Au thermoreflectance to phonon vs. electron temperature is a strong function of wavelength. We show that the commonly used two temperature model is not in agreement with our experimental data when the probe wavelength is in the visible. We credit this disagreement to nonthermal hot electron effects that are neglected by the two-temperature model. Our results will be useful for experimental studies of nonequilibrium heat transfer in metal multilayers.

I. Introduction.— The dielectric function of a metal describes the response of charge to light. The response is due to transitions between electronic states. The transitions can be between states in the same electronic band (intraband) or between states in different electronic bands (interband). Both types of transitions are sensitive to changes in the temperature of electrons and phonons. These transitions are sensitive to temperature for the following reasons [1].

i.   Volume thermal expansion decreases the plasma frequency and causes shifts and warping in the electron energy bands through changes in the one-electron potential. Changes in the bands cause the Fermi level to shift.

ii.   If the metal is a thin-film constrained by the substrate, thermal expansion also causes shear strains. Shear strains can split degenerate energy bands and cause shifting and warping as well. Warping can affect the Fermi level.

iii. The phonon population increases. This decreases electron relaxation times and shifts and warps the energy bands through the electron-phonon interaction.

iv.   The Fermi distribution broadens with increasing temperature. This affects all interband transitions that originate or terminate on states near the Fermi level.

v.   The electron-electron scattering rates increase with increasing temperature. This is a small effect, but may not be negligible. The role of electron-electron scattering is analyzed carefully in: "Electron-electron scattering in the intraband optical conductivity of Cu, Ag, and Au" by Beach and Christy, Physical Review B, 1977[2]. It is also discussed in a more recent paper by Pat Hopkins, "Influence of electron-boundary scattering on thermoreflectance calculations after intra- and interband transitions induced by short-pulsed laser absorption."[3].

vi.   The Fermi level increases even for a free electron gas, but this is a small effect.

vii.   If the temperature change is brought about by a current flow through the sample, the current flow displaces the distribution function in k-space. This change in distribution will affect interband transitions that originate or terminate on states near the Fermi level.

These seven origins of the thermoreflectance imply that the thermoreflectance will not be equally sensitive to changes in electron vs. phonon temperature. For example, volume thermal expansion (i) occurs primarily because of increases in phonon temperature [4]. Reasons (iii) and (iv) are describe direct effects of phonon vs. electron temperature increases, respectively. Furthermore, the strength of these various effects can be expected to depend strongly on wavelength. For example, changes in the Fermi-distribution due to electron temperature changes will matter most for wavelengths the excite transitions that originate / terminate at the Fermi level. Therefore, we expect the thermoreflectance sensitivity to phonon vs. electron temperature to be a strong function of wavelength.

The goal of this work is to measure how the thermoreflectance depends on the temperature of phonons vs. electrons in a simple metal. To do this, I perform wavelength dependent TDTR experiments of a thin 60 nm Au film. We choose Au as a model system to study because the d-band is located ~2.4 eV below the Fermi level, see Fig. 3.1. As a result, we expect the thermoreflectance to be very sensitive to the electron temperature near 2.4 eV (reason iv). Alternatively, in the infrared, Au behaves like a free electron metal and we expect thermoreflectance to be dominated by the phonon temperature (reason (iii)).

II. Experimental Methods.— In a TDTR experiment, the Au film is irradiated with a pump pulse. Then a time-delayed probe pulse measures pump induced changes in the reflectance. Details of our TDTR setup can be found in Chapter 1. In the first few picoseconds after laser excitation, the electrons and phonons have different temperatures. We hypothesis that the resulting time-evolution of the electron and phonon temperatures will cause a time evolution of the reflectance given by,

$$\Delta R(t) = \frac{\partial R}{\partial T_e} \Delta T_e(t) + \frac{\partial R}{\partial T_p} \Delta T_p(t) = \alpha_\lambda \Delta T_e(t) + \beta_\lambda \Delta T_p(t).$$ (3-1)

Here, R is reflectance, t is time after pump excitation, T_p is the phonon temperature, and T_e is the electron temperature. To determine α_λ and β_λ, we compare our data for $R(t)$ to the predictions of a two-temperature model for ΔT_p and ΔT_e while treating α_λ and β_λ as fitting parameters.

We prepared an 60 nm thick Au film via DC magnetron sputtering on a c-cut sapphire substrate. Prior to deposition, the sapphire substrate was heated in high vacuum to 650 C to clean the substrate surface. The substrate was then allowed to cool to room temperature in high vacuum and the Au was sputtered at 3.5mTorr pressure of Argon. To predict the time evolution of the electron and phonon temperatures in our Au film after laser excitation, we follow Ref. [5] and use the well-known two temperature model.

$$C_e \frac{\partial T_e}{\partial t} = \Lambda_e \frac{\partial^2 T_e}{\partial z^2} + g_{ep}\left(T_p - T_e\right) + P(t,z) ,$$ (3-2)

$$C_p \frac{\partial T_p}{\partial t} = \Lambda_p \frac{\partial^2 T_p}{\partial z^2} + g_{ep}\left(T_e - T_p\right).$$ (3-3)

We set the phonon heat capacity of Au to C_p = 2.45 MJ m^{-3} K^{-1} based on literature values [8].

We set the phonon thermal conductivity of Au to $\Lambda_p \approx$ 3 W m^{-1} K^{-1} based on the Leibfried Schlomann equation [7]. We set the electronic heat-capacity to $\gamma_e T_e$ with $\gamma_e \approx$ 68 J m^{-3} K^{-2} [6].

We set the thermal conductivity of the Au electrons to $\Lambda_e \approx$ 100 W m^{-1} K^{-1} based on four-point resistivity measurements and the Wiedemann-Franz law. We calculate $P(t,z)$ for Au using a

multilayer optical calculation and the literature values for the index of refraction of Au and sapphire. The only unknown parameter is g_{ep}. We then use Eq. (3-1) to compare the predictions of Eqs. (3-2) and (3-3) for T_e and T_p to our experimental data. We treat g_{ep}, α_λ and β_λ as fit parameters, with the constraint that g_{ep} be independent of wavelength. We show the predicted electron and phonon temperatures in Fig. 3.2 for an absorbed pump laser fluence of 1 J m^{-2} and $g_{ep} \approx 2 \cdot 10^{16}$ W m^{-3} K^{-1}.

III. Experimental Results.— We performed TDTR measurements with varied probe photon energy between 1.28-1.77 and 2.41-3.1 eV. During these experiments, the pump photon energy also varied between 1.28 and 1.77 eV. In the infrared, the pump photon energy is always equal to the probe photon energy. Alternatively, for probe energies between 2.41-3.1 eV, the pump energy is half the probe energy.

The results of these measurements are shown in figures 3.3-3.5, along with the best fit to our model described above. Table 3.1 compiles the resulting contributions from α and β vs probe energy in eV. In our study, we are not interested in the absolute magnitude of dR/dT vs. λ, which is determined by magnitude of α_λ of β_λ. Instead, we are interested in finding a method to independently measure the electron vs. phonon temperature, i.e. we are interested in $\alpha_\lambda / \beta_\lambda$. To simplify comparisons between data at various wavelengths, we normalized all data so that the $\Delta R(t = 10 \text{ ps}) = 1$. This normalization imposes the constraint that $\alpha_\lambda + \beta_\lambda = 1$.

In the infrared, we find that β α, i.e. the thermoreflectance is primarily determined by the phonon temperature. This is consistent with the dominant contribution to thermoreflectance being decreases in electron relaxation times and shifts. As the probe energy increases, sensitivity to the electron temperature increases. β / α decreases by a factor of ten between 1.2 and 1.8 eV.

For probe energies between 2.4 and 3.1 eV, the situation is more complicated. Unlike in the infrared, β is not always much larger than α. Furthermore, for some probe energies it is not possible to achieve good agreement between the model predictions and data, regardless of how α_λ and β_λ are adjusted. We credit this to the assumption inherent in the two-temperature model that the distribution of excited electrons is well described by a single temperature, T_e. More accurate modelling predicts the distribution will be nonthermal [9]. Recent work by Heilpern *et al.* suggest that $\Delta R_\lambda(t)$ measurements near the interband transition of Au can be used to directly measure the hot electron distribution. While nonthermal modelling and inversion of $\Delta R_\lambda(t)$ is beyond the scope of the current work, our results to date demonstrate that wavelength dependent TDTR can be a powerful tool for studying nonequilibrium heat transfer in nanoscale metal multilayers.

IV. Summary.— I have presented my experimental results and thermal models in order to deconvolute the contribution of electron and phonon changes in temperature to the thermoreflectance. By conducting TDTR measurements on 60nmAu/sapphire as a function of probe energy, the measurements show changes in respective sensitivities of electron and phonon temperatures due accessibility of interband transitions arising from the position of the d band, as opposed to predominantly intraband driven thermoreflectance. By assembling the sensitivity scaling factors regarding the electron and phonon contribution as a function of wavelength, a more in depth look at thermoreflectance can serve as a resource for heat transfer experiments on ps time scales and ns length scales.

V. Figures and Tables.—
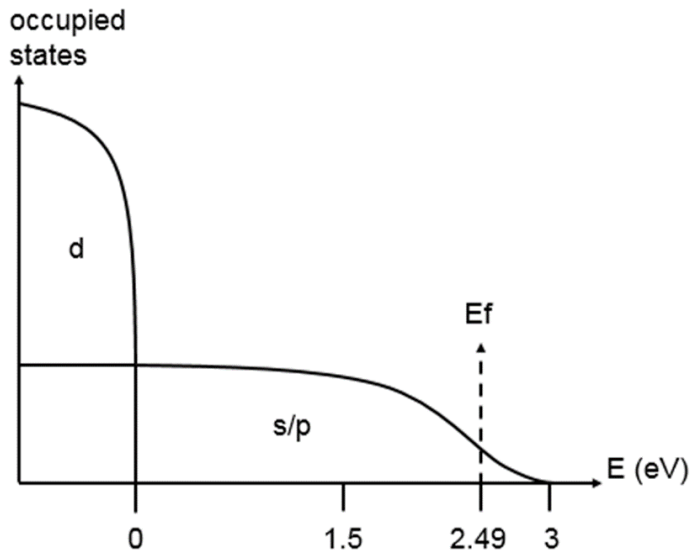
Figure 3.1. S/p and d band occupied states of Au as a function of energy. As the energy of the reflected light (probe light) increases towards the Fermi energy, 2.49eV, the probability increases of causing a transition from the d band which would alter the contribution to the thermoreflectance. Below 2.49eV it is much more probable that the reflectance is dependent on the s/p intraband transitions pertaining to a predominantly phonon contribution to the thermorefltectance.
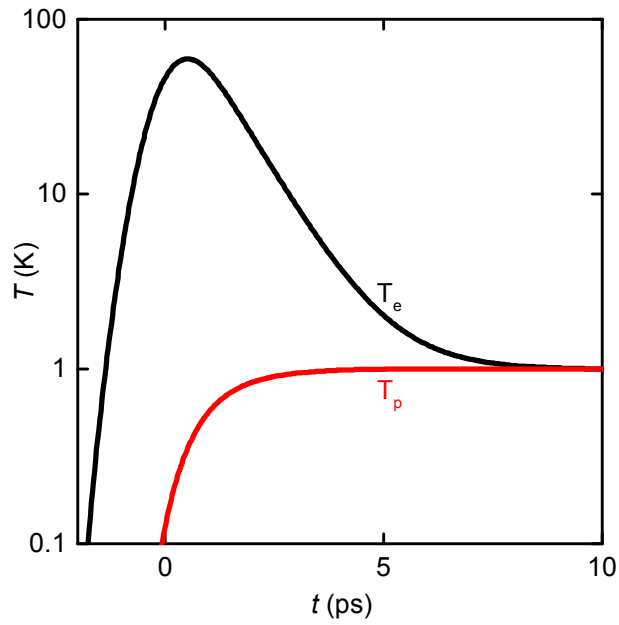
Figure 3.2. Thermoreflectance models of the electron temperature and phonon temperature in 60nmAu/sapphire after femto-second laser pulse heating. These temperature profiles were used to generate the model predictions for wavelength dependent TDTR measurements, save for the sensitivity scaling factors that the experimental data illuminated.
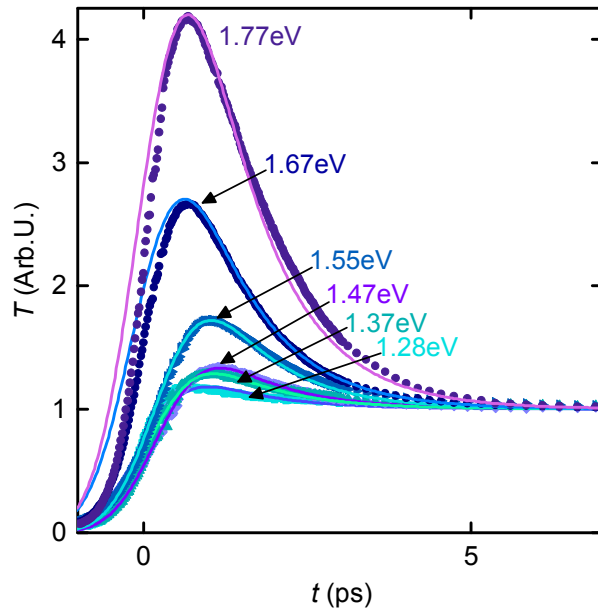
Figure 3.3. Thermoreflectance data and models of a 60nmAu/Sapphire sample. TDTR measurements were carried out as a function of probe energy in order to fit the scaling factor for the themoreflectance dependence on the electron and phono temperature. Experimental data and fits ranging from 1.28 to 1.77eV allow for the deconvolution of the electron and phonon contributions in this range.
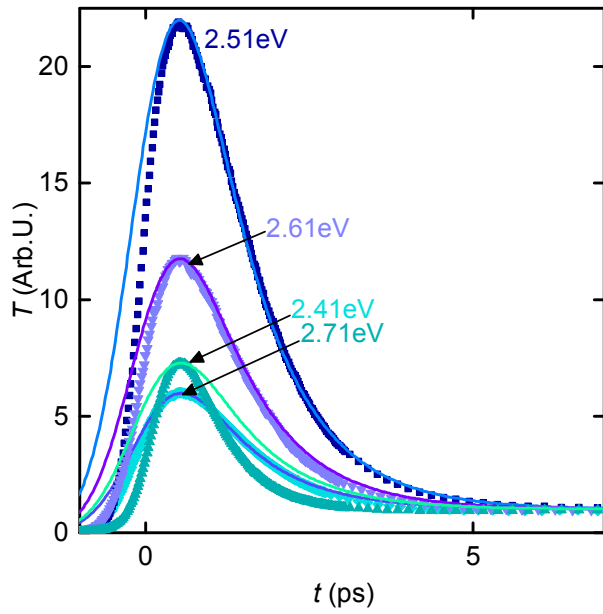
Figure 3.4. Thermoreflectance data and models of a 60nmAu/Sapphire sample. TDTR measurements were carried out as a function of probe energy in order to fit the scaling factor for the themoreflectance dependence on the electron and phono temperature. Experimental data and fits ranging from 2.71 to 3.1eV allow for the deconvolution of the electron and phonon contributions in this range.
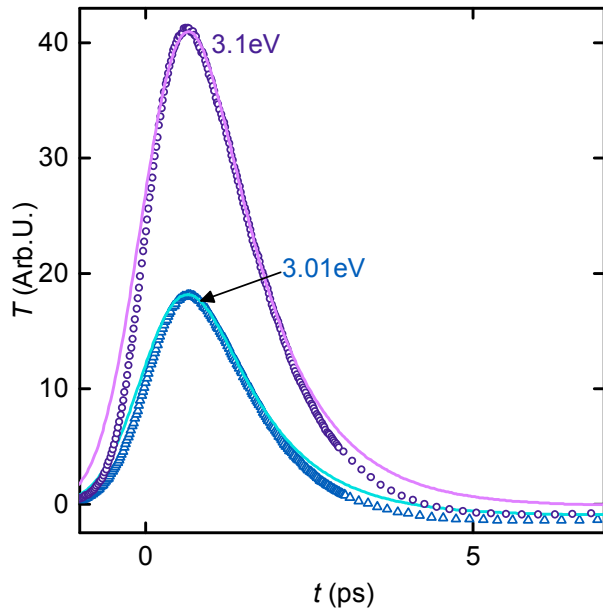
Figure 3.5. Thermoreflectance data and models of a 60nmAu/Sapphire sample. These two experimental plots were carried out at 3.01 and 3.1eV with the thermoreflectance signal dipping down into the negative regime of the y-axis, though near the thermal model prediction at 10ps.

Probe energy (eV)	α	β	β/ α
1.28	0.0126	0.9874	78.3651
1.37	0.0148	0.9852	66.5676
1.47	0.0157	0.9843	62.6943
1.55	0.0231	0.9769	42.2900
1.67	0.0411	0.9589	23.3309
1.77	0.0680	0.9320	13.7059
2.41	0.1000	0.9000	9.0000
2.51	0.3800	0.6200	1.6316
2.61	0.2020	0.7980	3.9505
2.71	0.1230	0.877	7.1301
3.01	-.3400	1.3400	-3.9412
3.1	-4.7000	5.7000	-1.2128

Table 3.1. Sensitivity scaling factors and the ratio of the two relating the thermoreflectance contribution from electron and phonon temperatures in 60nmAu/sapphire. α being the sensitivity scaling factor for the electron temperature contribution to the thermoreflectance, while β relates to the phonon contribution.

References

1.   R. Rosei and D. W. Lynch, "Thermomodulation Spectra of Al, Au, and Cu," Phys. Rev. B 5(10), 3883–3894 (1972).

2.   Electron-electron scattering in the intraband optical conductivity of Cu, Ag, and Au" by Beach and Christy, Physical Review B, 1977

3.   Pat Hopkins, "Influence of electron-boundary scattering on thermoreflectance calculations after intra- and interband transitions induced by short-pulsed laser absorption."

4.   Ashcroft, N. W. and N. D. Mermin (2010). "Solid state physics (saunders college, philadelphia, 1976)." Appendix N.

5.   Cahill, D.G., Analysis of heat flow in layered structures for time-domain thermoreflectance. Review of Scientific Instruments, 2004. 75(12): p. 5119-5122

6.   Lin, Z., et al. (2008). "Electron-phonon coupling and electron heat capacity of metals under conditions of strong electron-phonon nonequilibrium." Physical Review B 77(7): 075133.

7.   Wilson, R. B., et al. "Two-channel model for nonequilibrium thermal transport in pump-probe experiments." *Physical Review B* 88.14 (2013): 144305.

8.   Choi, Gyung-Min, R. B. Wilson, and David G. Cahill. "Indirect heating of Pt by short-pulse laser irradiation of Au in a nanoscale Pt/Au bilayer." *Physical Review B* 89.6 (2014): 064307.

9.   Tas, Guray, and Humphrey J. Maris. "Electron diffusion in metals studied by picosecond ultrasonics." *Physical Review B*49.21 (1994): 15046.

CHAPTER 4
Heat Transport Nanoscale Metal Multilayers

Super-Diffusive Heat Transport in Nanoscale Metal Multilayers

Thermal transport methods within nanoscale metal systems after ultra-fast laser pulses are not well understood. Specifically, it is not known how far heat travels away from a metal surface in the first few picoseconds after laser excitation. In the first picoseconds after laser excitation, electron-electron, and electron-phonon scattering produces a highly complex cascade of energy transfer. The complexity of this ultra-fast scattering reduces the clarity of the subsequent energy transfer throughout the metal system. We investigated Au/AuCoML(Multilayer) and Au/Cu/AuCoML samples via time-dsomain thermoreflectance (TDTR) and time-resolved magneto optic Kerr effect (TR-MOKE) measurements. By conducting several pump-probe experiments, we are able to develop a more clear understanding of how energy absorbed at the surface disperses throughout the metal multilayer system on nm length, and ps time-scales. Our results suggest transport is not exclusively diffusive or ballistic. Instead, some hot electrons carry energy ballistically, while others carry energy diffusively, i.e. transport is super-diffusive.

I. Introduction. — Understanding heat transport due to femto-second laser pulse heating in metal multilayer systems may allow for new types of information technologies. Ultrafast laser heating of magnetic multilayer systems produces radiation in elusive frequency domains, 1THz-100THz. Furthermore, Hot electron transport in metal systems can generate spin transfer torque (STT) between magnetic metal layers, providing opportunities for writing magnetic information. Ultrafast heating of magnetic metals can allow switching of the the magnetic moment of film on ps time scales. While these results show great promise and point the way for further investigations, a fundamental description of how the energy deposited in these systems is transported on these ultra-fast time scales has yet to be agreed upon by the scientific community.

Ultrafast heating of metals causes enormous spatial gradients in energy density. Hot electrons will disperse rapidly to relax these gradients. The typical time-scale for electron-phonon relaxation is ~ 1 ps. If hot electrons carry heat ballistically for 1 ps with a Fermi velocity of $v_f \approx 10^6$ m/s, the distance heat travels is $d \approx v_f \tau_{ep} \approx 1\,\mu m$. Alternatively, if hot electrons carry heat diffusively for 1 ps with a thermal diffusivity of $D_e \approx 10^{-4}$ m^2 s^{-1}, then $d \approx \sqrt{D_e \tau_{ep}} \approx 0.1\,\mu m$. A third option is that both ballistic and diffusive transport are important and the heat-transfer is superdiffusive [21-24]. In a superdiffusive regime, the distance d that heat travels in time t is $d \propto t^\alpha$, where $0.5 < \alpha < 1$. $\alpha = 1$ represents the ballistic limit, $\alpha = 0.5$ the diffusive limit.

To date, experimental studies of how heat evolves in space after ultrafast optical excitation are inconclusive. Time of flight measurements suggests that at least some heat-transfer is ballistic on length-scales as large as 300 nm [25, 26]. Alternatively, several recent experimental studies conducted suggest that heat-transfer is sometimes well described by a diffusive two-temperature model [27, 28]. Another set of experimental studies explains observations with a superdiffusive transport model [25, 29]. Choi et al provide pump-probe experimental results and show that a

diffusive model describes heat transport in their Cu/PtCoML system, while Bergeard et al use similar experiments showing that a ballistic transport model is in gohod agreement with their experimental results. Currently, no clear criteria exist for when heat transfer will be diffusive, superdiffusive, or ballistic.

By conducting a combination of Time-Domain Thermoreflectance measurements (TDTR) and Time-Resolved Magneto-Optic Kerr Effect Measurements (TR-MOKE) we quantify the distance energy is transported by hot electrons in a Au and Cu layer before thermalizing with the phonons. In Au, the hot electrons travel ~60 nm further than diffusive theory predicts, which may be a signature of superdiffusive transport. In Cu, hot electron transport is significantly different than in Au despite similar thermal properties. The differences between Au and Cu demonstrate the necessity of using microscopic transport models for describing energy transfer in nanoscale metal systems.

II. Sample preparation.—In our measurements, we use the ultrafast magnetic moment of nm thick Co layers as a thermometer. In order to conduct our polar TR-MOKE experiments, the thin Co layers need to have perpendicular magnetic anisotropy (PMA). This is because our polar MOKE measurements are only sensitive to the out of plane component of the magnetic moment.

We prepared our sample in a high vacuum chamber via DC magnetron sputtering at 3.5 mTorr at a power of 10 W for Au layers, 20W for Co layers, and 200W for Cu layers. Samples were sputtered onto sapphire. Simultaneously, we also sputtered dummy films on BK7 glass for use as a reference sample. Substrates were heated in vacuum to 200C for 1 hour to produce a clean substrate surface and the substrate was then allowed to cool in vacuum to room temperature. At room temperature, a Ta seed layer was sputtered onto the substrates, followed by the AuCoML, and finally with an Au or Au/Cu capping layer. The samples were then annealed at 145C for 30min in order to increase the mobilities of the respective metals and thus sharpen the AuCoML interfaces

which produces strong PMA due to interfacial contributions to the magnetic moment. Sample thicknesses were characterized via TDTR picosecond acoustic and beam deflection measurements.

III. Experimental Methods. — TR-MOKE and TDTR measurements were conducted as a function of Au thickness and probe energy. Prior studies of similar systems with TDTR and/or TR-MOKE measurements performed measurements at only a single wavelength . The goal of these prior experiments was to directly measure the time-of-flight for energy to traverse the film. Our goal is different. We want to use a combination of thermometry methods to determine the spatial distribution of energy after electron-phonon thermalization.

After absorption of the femto-second laser pulse near the surface of the metal layer (approx. 10nm penetration depth), a diffusive two temperature model predicts that hot electrons diffusive ~ 80 nm before thermalizing with phonons. Alternatively, if hot electron transport is purely ballistic hot electrons should be able to traverse as far as ~1 μm, and heat will be evenly distributed across the multilayer after 1 ps. If some electrons carry heat ballistically, while others transport heat diffusively, heat transfer is known as superdiffusive. For superdiffusive transport, we expect energy to be distributed across a greater length-scale than 80 nm, but a smaller length scale than 1 μm.

To determine the length-scale over which energy is deposited while electrons are hot, we measure the time-evolution of the Co film temperature in response to optical heating of the opposite side of the multilayer (Au surface). We track the Co film temperature on time-scales from 3 ps to 10 ns via TR-MOKE measurements of the change in magnetic moment, which is proportional to the change in temperature. The virtue of analyzing the data on time-scales longer than 3 ps is that, on these time-scales, we know heat is transported diffusively. All existing theories for hot electron dynamics agree that electron-electron and electron-phonon scattering drive the photoexcited electron distribution to a thermalized Fermi-Dirac distribution within the first few picoseconds after laser excitation. While transport on time-scales from 3 ps to 10 ns is neither ballistic nor

superdiffusive, this approach still provides critical insight into how far heat is transported in the first few picoseconds after laser excitation. The temperature evolution of the thin Co films depends strongly on how energy is distributed across the multilayer after hot electron thermalization. Therefore, the time-evolution of the Co film temperature allows us to uniquely determine the distance hot electrons travel in the Au layer in the first few picoseconds after laser excitation.

In addition to TR-MOKE measurements of the Co temperature evolution, we also conduct TDTR measurements of the time-evolution of the Au surface on the opposite end of the multilayer. We peform TDTR experiments at both 1.3 eV and __ eV. This allows us to discern between the electron and phonon temperature in the Au due to changes from intraband to interband transitions.

IV. Experimental Results. We investigate the possibility of super-diffusive transport by conducting several pump probe experiments, pumping Au in Au/AuCoML samples and either probing Au with TDTR or AuCoML with TR-MOKE to provide spatial resolution to our findings. We conducted three main measurements, with one supplemental measurement needed to remove any free parameters from our experiments.

TR-MOKE measurements were also conducted in which the Au layer was pumped and the AuCoML was probed. The TR-MOKE measurement was then fit with a modified diffusive model described by equations 1 and 2.

$$C_e \frac{\partial T_e}{\partial t} = \Lambda_e \frac{\partial^2 T_e}{\partial z^2} + g_{ep}\left(T_p - T_e\right) + P(t,z) \;,\; (1)$$

$$C_p \frac{\partial T_p}{\partial t} = \Lambda_p \frac{\partial^2 T_p}{\partial z^2} + g_{ep}\left(T_e - T_p\right). \; (2)$$

The modification came by retaining the very well understood diffusive model, but making an assumption that the energy is deposited 60nm into the Au layer. This is physically incorrect as Maxwell's equations describe very well that the absorption occurs at these wavelengths within the

63

first 10nm or so. What this assumption allows us to do is to retain the robustness of the diffusive model, while assuming that the hot electrons actually promoted in the first 10nm of the Au then behave ballistically for 60nm before the heat transport behaves diffusively. As shown in Fig. 4.1, change in temperature of the AuCoML via TR-MOKE at 1.58eV probe energy were measured as a function of Au film thickness. We then fit the experimental data with the modified diffusive model, shown in equation 1 and 2. We also fit the experimental data with both diffusive and ballistic models, though neither were in good agreement with the data. I also conducted the same TR-MOKE measurements with the same AuCoML magnetic multilayer, while changing the capping Au film to 30nmAu/220nmAu overlaying the AuCoML. Fig. 4.2 shows that while the 230nmAu/AuCoML sample is very similar in thickess to the CuAu sample, a noticeable decrease in temperature rise vs time is present. This gives testament that although Cu and Au have very similar thermal properties, the heat transport in these two samples produce different transport behaviors, which is non-intuitive to the heat transport community. Futher similar experiments as a function of metal layer would help to understand dependent variables not currently described at a fundamental level, such as scattering effects in the different metals.

To describe the thermoreflectance of Au we conducted TDTR measurements as a function of probe energy on 60nmAu/sapphire, more thoroughly discusses in chapter 3, where the thermoreflectance is related eq 3.

$$\Delta R = \alpha \Delta T_e + \beta \Delta T_{ph}, \qquad (3)$$

Because of this supplemental experimentation, we were then able to perform TDTR measurements, pumping the Au and probing the Au as a function of wavelength and thickness of Au to describe the electron and phonon temperatures in the more complicated structure of Au/AuCoML shown in Fig.4.3 at 3.1eV probe energy and Fig. 4.4 at 1.28eV probe energy, corresponding to the electron and phonon temperatures in the Au, respectively. By then fitting the

experimental data with the same super-diffusive model used in the TR-MOKE experiment, save

for the experimental findings of $\alpha \, and \, \beta$ used to account for the thermoreflectance contributions

as per equation 3. Our thermal mode fits well, as shown in Fig. 4.3 and 4.4, showing the

robustness of out modified diffusive model (super-diffusive model), to changes in experiment,

changes in probe energy, and changes in probe location (Au side of AuCoML side).

V. Summary. — I have presented my experimental results and thermal models in order to

illuminate the heat transport behavior in nanoscale metal multilayers on ps time scales after femto-

second laser absorption. By neither using a classical diffusive model, or ballistic mode, but rather

modifying the well known diffusive model to account for hot electron transport of 60nm in Au, I

was able to fit with good agreement 3 different sets of experiments with different probe energies,

probe locations (Au vs AuCoML side) and experimental methods (TDTR vs TR-MOKE), also

showing that materials with similar thermal properties (Au and Cu) do not necessarily perform

similarly with regards to their heat transport behaviors. This work may serve as a resource for

furthering the discussion between the highly complex nature of heat transport on these systems.

Figure 4.1. TR-MOKE data and model prediction related to change in temperature in Au/AuCoML as a function of Au capping layer thickness. Pumping the Au layer and probing the AuCoML side at 1.58eV probe energy shows the temperature change regarding increasing Au thickness. Modified diffusive model predictions show that a ballistic length of 60nm produces a fit in good agreement, while there are no other free parameters other than the ballistic length.
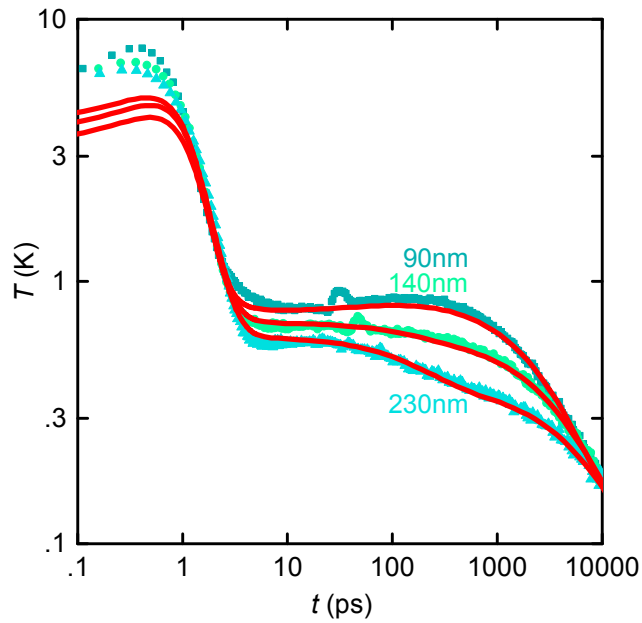
Figure 4.2. TDTR data and model prediction related to change in temperature in Au/AuCoML as a function of Au capping layer thickness. Pumping and probing the Au layer with a probe energy of 3.26eV shows the temperature change regarding increasing Au thickness. By studying the TDTR dependence on electron and phonon contributions we are able to have no free parameters in the model prediction, and accounting for the change in probe energy we use the same fit as figure 4.1 and our data is still in good agreement.
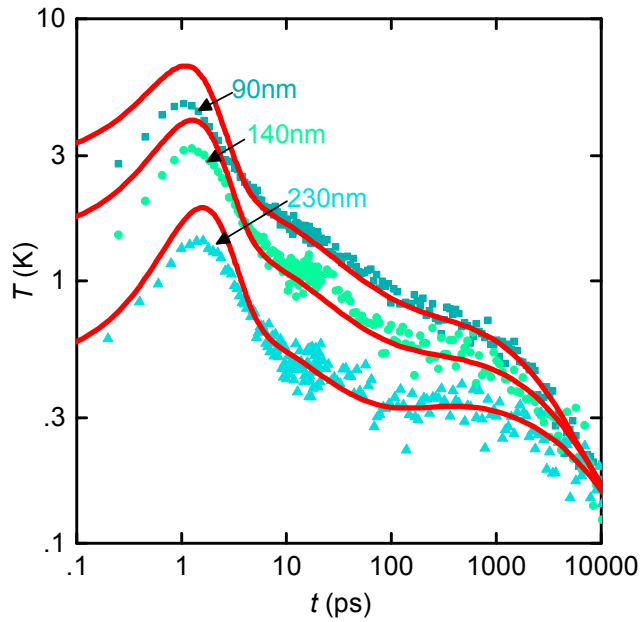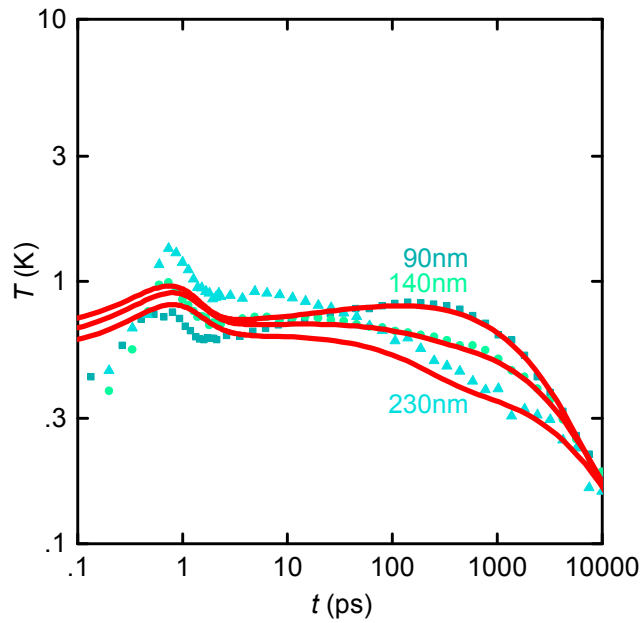
Figure 4.3. TDTR data and model prediction related to change in temperature in Au/AuCoML as a function of Au capping layer thickness. Pumping and probing the Au layer with a probe energy of 3.1eV shows the temperature change regarding increasing Au thickness. Again accounting for the change in thermorecflectance contributions for the change in probe energy we use the same fit as figure 4.1 and 4.2. Short time delays show some lack of agreement with the model and this may be due to unexpected electron contribution to the thermoreflectance. This being the case, out model prediction is still in fairly good agreement.
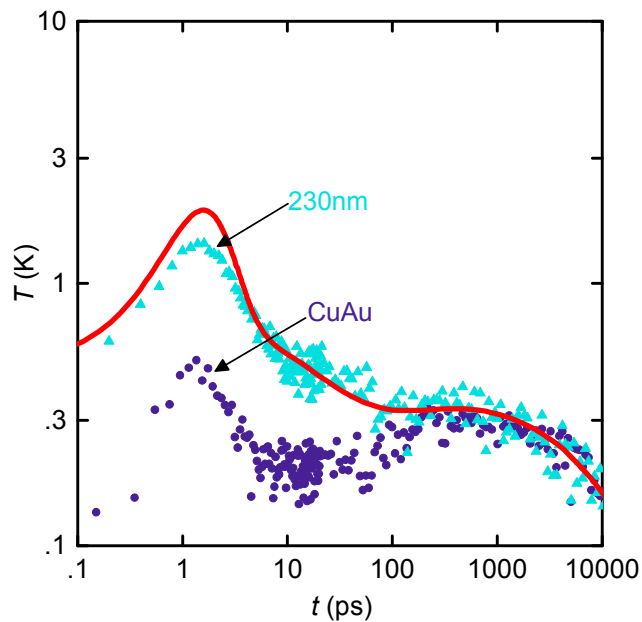
Figure 4.4. TR-MOKE data and model prediction from experimental data for 230nmAu/AuCoML shown in figure 4.1, with 30nmAu/220nmCu/AuCoML shown in purple diamonds. Given nearly identical capping layers of approximately 230nm, the temperature change between the two samples are drastic. Changes in capping layer from Au to Cu would not intuitively suggest such a temperature difference between the two samples. This suggests that even very similar metals can provide complexities in heat transport and that my experimental methods may be used in future works to conduct material dependent scans further illuminating the nature of heat transport in these systems.

.

References

1.   Cahill, D.G., *Analysis of heat flow in layered structures for time-domain thermoreflectance.* Review of Scientific Instruments, 2004. **75**(12): p. 5119-5122.

2.   Wilson, R., et al., *Thermoreflectance of metal transducers for optical pump-probe studies of thermal properties.* Optics express, 2012. **20**(27): p. 28829-28838.

3.   Hohensee, G.T., et al., *Interpreting picosecond acoustics in the case of low interface stiffness.* Review of Scientific Instruments, 2012. **83**(11): p. 114902.

4.   Yang, Y., et al., *Ultrafast magnetization reversal by picosecond electrical pulses.* Science Advances, 2017. **3**(11).

5.   Rost, C.M., et al., *Hafnium nitride films for thermoreflectance transducers at high temperatures: Potential based on heating from laser absorption.* Applied Physics Letters, 2017. **111**(15): p. 151902.

6.   Jiang, P., X. Qian, and R. Yang, *A new elliptical-beam method based on time-domain thermoreflectance (TDTR) to measure the in-plane anisotropic thermal conductivity and its comparison with the beam-offset method.* arXiv preprint arXiv:1803.06551, 2018.

7.   Li, M., J.S. Kang, and Y. Hu, *Anisotropic thermal conductivity measurement using a new Asymmetric-Beam Time-Domain Thermoreflectance (AB-TDTR) method.* Review of Scientific Instruments, 2018. **89**(8): p. 084901.

8.   Sun, B. and Y.K. Koh, *Understanding and eliminating artifact signals from diffusely scattered pump beam in measurements of rough samples by time-domain thermoreflectance (TDTR).* Review of Scientific Instruments, 2016. **87**(6): p. 064901.

9.   Chen, J.-Y., et al., *Time-resolved magneto-optical Kerr effect of magnetic thin films for ultrafast thermal characterization.* The journal of physical chemistry letters, 2016. **7**(13): p. 2328-2332.

10.   Kang, K., et al., *Two-tint pump-probe measurements using a femtosecond laser oscillator and sharp-edged optical filters.* Review of Scientific Instruments, 2008. **79**(11): p. 114901.

11.   Heilpern, T., et al., *Determination of hot carrier energy distributions from inversion of ultrafast pump-probe reflectivity measurements.* Nature communications, 2018. **9**(1): p. 1853.

12.   Khorsand, A.R., et al., *Element-Specific Probing of Ultrafast Spin Dynamics in Multisublattice Magnets with Visible Light.* Physical Review Letters, 2013. **110**(10): p. 107205.

13.   Visnovsky, S., et al., *Magneto-optical effects in Au/Co/Au ultrathin film sandwiches.* Journal of magnetism and magnetic materials, 1993. **128**(1-2): p. 179-189.

14.   Jakubisova-Liskova, E., et al., *Optical spectroscopy of sputtered nanometer-thick yttrium iron garnet films.* Journal of Applied Physics, 2015. **117**(17): p. 17B702.

15.	Tas, G. and H.J. Maris, *Electron diffusion in metals studied by picosecond ultrasonics.* Physical Review B, 1994. **49**(21): p. 15046.

16.	Devos, A. and A. Le Louarn, *Strong effect of interband transitions in the picosecond ultrasonics response of metallic thin films.* Physical Review B, 2003. **68**(4): p. 045405.

17.	Hamrle, J., et al., *In-depth resolution of the magneto-optical Kerr effect in ferromagnetic multilayers.* Physical Review B, 2002. **66**(22): p. 224423.

18.	Schellekens, A.J., et al., *Exploring laser-induced interlayer spin transfer by an all-optical method.* Physical Review B, 2014. **90**(10): p. 104429.

19.	Hohlfeld, J., et al., *Femtosecond time-resolved reflection second-harmonic generation on polycrystalline copper.* Applied Physics A, 1995. **60**(2): p. 137-142.

20.	Hohlfeld, J., et al., *Electron and lattice dynamics following optical excitation of metals.* Chemical Physics, 2000. **251**(1-3): p. 237-258.

21.	Vermeersch, B., et al., *Superdiffusive heat conduction in semiconductor alloys. II. Truncated Lévy formalism for experimental analysis.* Physical Review B, 2015. **91**(8): p. 085203.

22.	Vermeersch, B., et al., *Superdiffusive heat conduction in semiconductor alloys. I. Theoretical foundations.* Physical Review B, 2015. **91**(8): p. 085202.

23.	Battiato, M., K. Carva, and P.M. Oppeneer, *Theory of laser-induced ultrafast superdiffusive spin transport in layered heterostructures.* Physical Review B, 2012. **86**(2): p. 024404.

24.	Battiato, M., K. Carva, and P.M. Oppeneer, *Superdiffusive spin transport as a mechanism of ultrafast demagnetization.* Physical review letters, 2010. **105**(2): p. 027203.

25.	Malinowski, G., et al., *Hot-electron transport and ultrafast magnetization dynamics in magnetic multilayers and nanostructures following femtosecond laser pulse excitation.* The European Physical Journal B, 2018. **91**(6): p. 98.

26.	Bergeard, N., et al., *Hot-electron-induced ultrafast demagnetization in Co/Pt multilayers.* Physical review letters, 2016. **117**(14): p. 147203.

27.	Wilson, R.B., et al., *Ultrafast magnetic switching of GdFeCo with electronic heat currents.* Physical Review B, 2017. **95**(18): p. 180409.

28.	Choi, G.-M., R.B. Wilson, and D.G. Cahill, *Indirect heating of Pt by short-pulse laser irradiation of Au in a nanoscale Pt/Au bilayer.* Physical Review B, 2014. **89**(6): p. 064307.

29.	Eschenlohr, A., et al., *Ultrafast spin transport as key to femtosecond demagnetization.* Nature materials, 2013. **12**(4): p. 332.

CHAPTER 5
Spin Accumulation in Au

Spin Accumulation in Au due to Femto-Second Demagnetization of AuCo Multilayers

Spin accumulation in Au following demagnetization of an adjacent nanoscale magnetic multilayer was studied as a function of probe energy and thickness of the Au spin sink. Time-Resolved Magneto Optic Kerr Effect (TR-MOKE) measurements were conducted as a function of probe energy, ranging from 2.4 to 3.26eV, to understand the sensitivity and structure of the resulting change in Kerr signal on ps time-scales. A 700fs Ti:Sapphire laser absorbed by the PMA layer results in a reduction in magnetic order proportional to the absorbed fluence. Conservation of angular momentum results in a spin current being injected into the adjacent non-magnetic layer (Au). The spin accumulation in the Au layer causes a rotation in the polarization of reflected light Our results for the Kerr spectra of Au are in reasonable agreement with density functional theory predictions.

I. Introduction. — When an ultra-fast laser pulse is absorbed by a magnetic layer, the increase in temperature causes electron spins to flip due to spin degrees of freedom. The magnetic layer's magnetization decreases proportional to the absorbed laser energy[2]. The rapid decrease in magnetic moment and spin disorder in the magnetic layer causes spin-current to be injected into any adjacent layers, e.g. non-magnetic metal (Au) due to a conservation of angular momentum. In Chapter 4, we report experimental measurements of heat-transfer in Au/AuCoML systems in order to better understand how excess energy provided by a femto-second laser is transported throughout nanoscale metal systems. Here, we focus on the same material system but perform experiments to quantify how spin is detected in the Au layer following spin-transport in these systems and do so via TR-MOKE.

The magneto optic response of Au has been experimentally measured at a few isolated wavelengths, but no systematic comparison between experiment vs. wavelength and model predictions currently exists. Several recent studies have successfully used the small MOKE signals that arise from spin accumulation in Au as a probe of optically generated spin currents. Here, by conducting TR-MOKE measurements as a function of probe energy we measure the Kerr angle of Au in the presence of spin accumulation vs. wavelength. We then compare our results to theory and find they are in reasonable agreement.

We utilize the same experimental system, described in our previous work (Chapter 1), to now describe how the change in Kerr rotation as a function of probe energy displays a change in both sensitivity and sign of rotation. Utilizing TR-MOKE measurements to understand spin accumulation in Au can be highly advantageous due to its capabilities for extremely low noise levels (see chapter 1), its sub ps time scale resolution, as well as the variability of the experiments possible with TR-MOKE [4,6]. By understanding the TR-MOKE response of Au as a function of

probe energy, and Au thickness, a resource for future experiments as well as spintronic devices can be obtained.

   II. Sample preparation.—Our Au/AuCoML samples, as shown in Fig. 5.6, were prepared via DC magnetron sputtering in a high vacuum chamber (AJA Orion) with the aid of a sample shutter. First the sapphire substrate was annealed in high vacuum at 850C for 5 minutes in order to remove any adsorbents from the sapphire surface. After letting the sapphire substrate cool to 28C, a Ta seed layer was sputtered onto the sapphire followed by the AuCoML. Then, a sample shutter was rotated over the sample so as to cover approximately 40% of the sample surface. Au was then sputtered onto the sample, where the Au sputter gun is angled at approximately 45 degrees to the sample surface. The combination of the Au sputter gun angle, and the sample shutter produced a gradient effect regarding the Au coverage. Au was thickest (approximately 400nm) where the sample was uncovered by the shutter, and the Au thickness decreased underneath the shutter, as fewer amounts of Au could cover the surface.

III. Experimental Methods. —As light is reflected off of a metal surface, in our case Au, it is reflected with some polarization. As the femtosecond laser causes disorder in the AuCoML spins, a spin current is injected into the Au. After a net magnetic moment is present in the the Au, due to the spin injection from the AuCoML, a torque is applied to the reflected light, causing a change in its polarization. This change in polarization is proportional to the change in magnetic moment in the Au, but the sensitivity of this change in magnetic moment in Au is not constant at all wavelengths. We utilize TR-MOKE measurements as a function of probe energy using our laser system (described in chapter 1) in order to investigate the sensitivity and sign of the magneto optic response to heating.

   The Ti:Sapphire laser emits a wavelength tunable from 690-1060nm and using a second harmonic generator, we are able to probe the Au layer at higher energies ranging from 2.4 to

3.26eV. As shown in Fig 5.6, the pump laser supplies the heat to the AuCoML magnetic layer and the spin current is injected into the Au layer where the probe reflects off of the Au and is torque due to the spin accumulation in the Au. Since our system is only sensitive to the polar MOKE response, that is the change in polarization is sensitive only to the change in magnetic moment out of plane, we set the magnetic moment of the AuCoML, which exhibits strong perpendicular magnetic anisotropy, using a 0.4T NdFeB magnet in between scans (magnet not present during scans). After probe light is reflected off of the Au sample, the collected light is split into orthogonal polarizations using a wollaston prism. The probe now split into two beams is focused onto a detector with two photodetectors. The signal is balanced between detectors using a half wave plate so that photodetector one and two are detecting identical intensities of light. The photodetectors are subtracted from one another and when no change in magnetic moment is present in the Au layer, the photodetectors remain balanced. After femtosecond heating creates a spin accumulation in the Au, the change in magnetic moment rotates the polarization of the probe light. Now the detectors will no longer be balanced as the light has been rotated more towards p or s polarization, and thus one photodetector will increase in signal and the other will decrease. This change is signal detected is relayed to a SRS lock-in and in which our system is able to detect rotations of light on the order of nanoradians (see chapter 1). By conducting these TR-MOKE measurements as a function of probe energy, we uncover the sensitivity and sign of the magneto optic Kerr response in Au

To investigate the TR-MOKE response Au after ultra-fast laser heating, we needed to first characterize the behavior of the reflected light with regards to any ensuing ellipticity since the MOKE is actually a combination of the ellipticity and polarization as shown in equation 1.

$$\Theta_K = \theta_k + i\varepsilon_k = r_{sp}/r_p = \left|r_{sp}\right|/\left|r_p\right|\left(\cos\left(\phi_{sp} - \phi_{pp}\right) + i\sin\left(\phi_{sp} - \phi_{pp}\right)\right). \qquad (1)$$

.

We were able to isolate the change in ellipticity and polarization by accounting for the Jones matrix representing our optical detection components. To do this we began having our laser setup in the Front-Back orientation as shown in Fig 5.6. This setup allows for the pump (heating laser) and probe (detection laser) to be incident on opposite sides of the sample, similar to Ref [6]. After the probe passes through the second harmonic generator, it is then passed through optical filters to remove any unwanted wavelengths, and then through a polarizer so that the probe light incident on the Au surface is p polarized so as to remove any ellipticity before the light has reached the Au surface. After the probe beam is reflected from the Au surface it is collected via a non-polarizing beam-splitter and a broadband dielectric mirror which are both angled at 45 degrees, so as to direct the light to our photodetector. In order to remove the ellipticity due to our optical components, the ellipticity induced via these two optical components needs to be accounted for and removed.

We made sure our experimental signal was only a measure of the real part of the Kerr angle via the use of a set of a birefringent crystal on a translation stage (Thorlabs Soleil-Babinot Compensator). This compensator fixes any ellipticity introduced by our detection path non-polarizing beam splitter and mirror. By moving the respective crystal positions in our compensator, we confirmed via a polarimeter (Thorlabs) that we were able to describe and remove the ellipticity introduced from our optical components. We obtained the respective crystal positions via a digital micrometer for the energy range of interest (2.4 to 3.26eV) and then conducted out TR-MOKE measurements to obtain the change in Kerr rotation component of the MOKE effect as a function of probe energy and Au thickness.

IV. Experimental Results.— By pumping the AuCoML and probing the Au, and varying the Au thickness as shown in Fig.5.6 we can see how much spin is diffused as a function of film thickness, in which this TR-MOKE experiment was carried out with a probe energy of 1.58eV. We do not see a linear decrease in the detected signal, but rather an exponential one due to the volumetric dispersal

of the spin current throughout the Au film and spin-flip scattering of the spin current. We also note a slight change in shape after a few ps as the thickness of the Au layer is decreased. In Fig.5.2 we see TR-MOKE scans of 170nmAu/AuCoML/sapphire, as a function of probe energy, with the pump incident on the AuCoML and the probe incident on the Au. Fig.5.3 we present the normalized maximum Kerr signal as a function of the entire scanned energy level. By comparing to model predictions of Au's behavior to change in Kerr signal, we see that out shape, change of sign, and relative magnitudes are in good agreement.

V. Summary.— I have presented my experimental results describing the method for obtaining the TR-MOKE response of Au due to spin accumulation as a function Au thickness and probe eV. I described the issues regarding ellipticity and how we were able to remove them from our system and obtain a highly structured TR-MOKE signal, showing changes of several orders in magnitude while also changing signs from positive to negative as the probe energy is increased. Model predictions of the structure of Au's magneto optic response are in good agreement with my results as is elusive in other works. This understanding of the detected signal may help to tailor spintronic devices and future experiments, by serving as a resource for where the TR-MOKE signal may be suppressed or maximized.
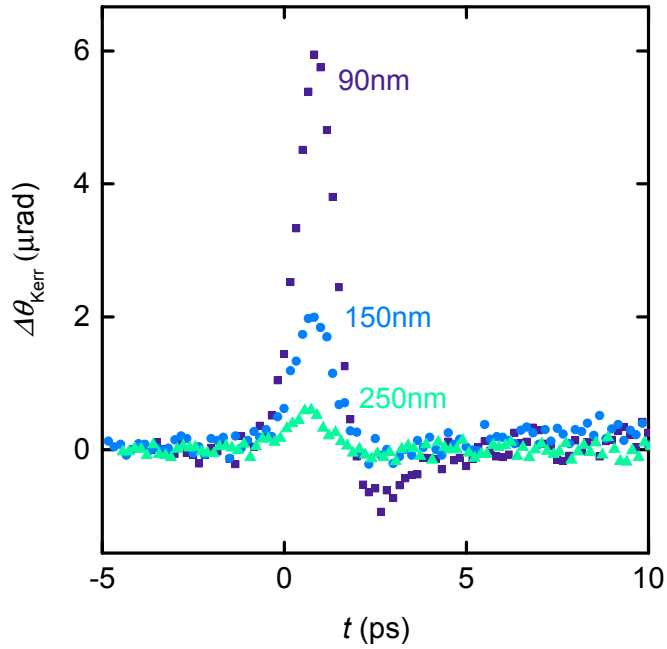
Figure 5.1. TR-MOKE results for Au/AuCoML as a function of capping Au layer thickness. Pumping the AuCoML side and probing the Au side of the sample, the spin current diffused through the Au is shown to be highly dependent on thickness at 90nm, 150nm, and 250nm of Au. Measurements for this experiment were conducted at 1.58eV and the data is normalized for absorbed fluence to discount changes in pump power.
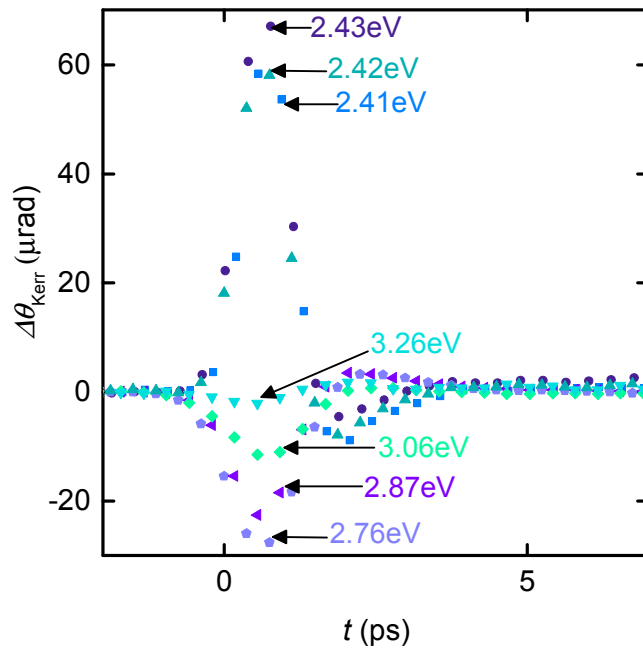
Figure 5.2. TR-MOKE results for Au/AuCoML as a function of capping probe eV layer. Pumping the AuCoML side and probing the Au side of the sample for 170nmAu/AuCoML, shows an interesting structure in the time evolution of spin accumulation. As can be seen, the sign and magnitude of the Kerr signal are highly dependent on probe energy.
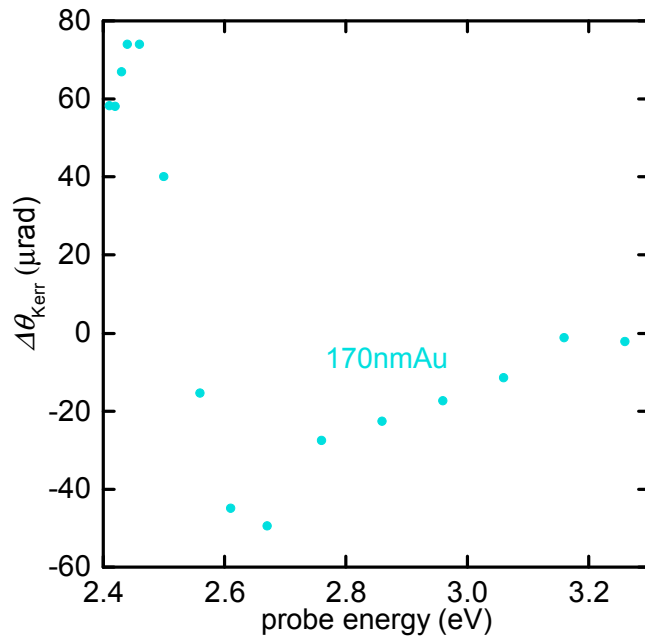
Figure 5.3. TR-MOKE data of Au/AuCoML showing change in Kerr angle as a function of probe energy, after femto-second demagnetization of the AuCoML spin source with the Au spin sink being 170nm thick. Experimental results show a highly structured signal with changes in magnitude as well as a switching of sign.
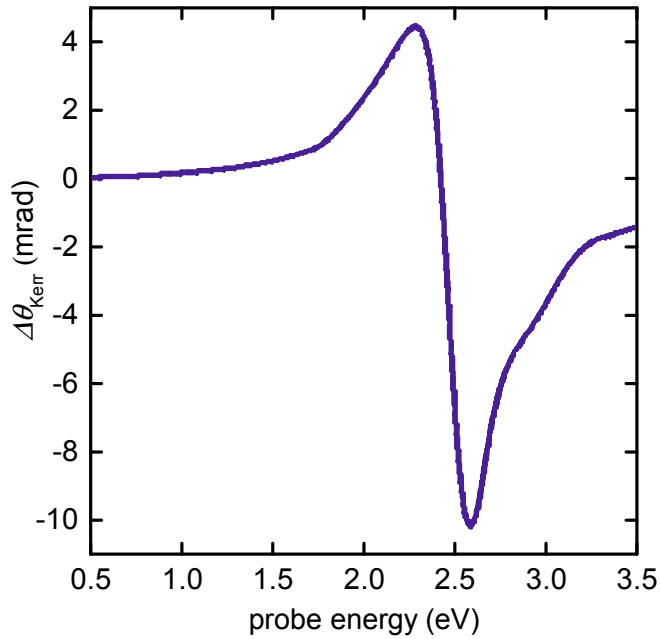
Figure 5.4. Model prediction of the sensitivity to the change in Kerr angle vs probe energy. By accounting for the material properties of Au, model prediction from 0.5 to 3.5eV were shown to predict a highly structured change in Kerr angle in Au. The model prediction showed large changes in magnitude of sensitivity to the signal, as well as changes in sign of the polarization rotation.
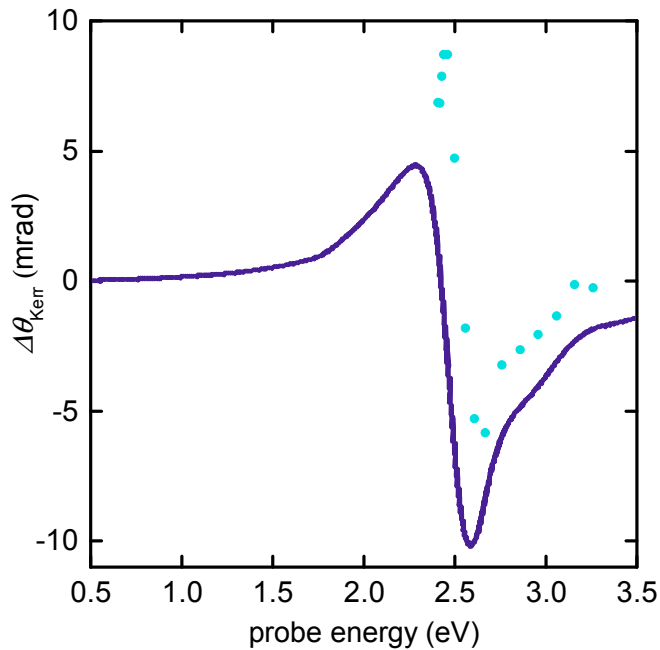
Figure 5.5. Model prediction of change in Kerr angle with experimental data scaled to fit. As can be seen, experimental results are in fairly good agreement with the model prediction as both exhibit a change in magnitude and sign at nearly identical probe energies.
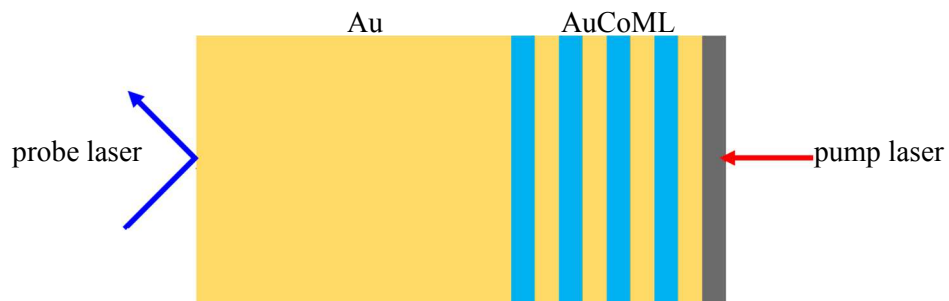

Figure 5.6. Geometry of the Au/AuCoML sample investigated with TR-MOKE. Here we see the pump laser incident on the AuCoML side of the sample causing demagnetization of the AuCoML due to spin degrees of freedom thus leading to a spin injection into the Au layer. The probe beam, wavelength varying from 1.58eV to 2.41-3.26eV, was incident on the Au layer and detected the spin accumulation via a change in polarization of the reflected probe.

.

References

1. Schellekens, A., et al. (2014). "Ultrafast spin-transfer torque driven by femtosecond pulsed-laser excitation." Nature communications 5: 4333.

2. Koopmans, B., et al. (2010). "Explaining the paradoxical diversity of ultrafast laser-induced demagnetization." Nature materials 9(3): 259.

3. Choi, G.-M., et al. (2015). "Thermal spin-transfer torque driven by the spin-dependent Seebeck effect in metallic spin-valves." Nature physics 11(7): 576.Qiu, Z. and S. D. Bader (2000).

4. Choi, G.-M., et al. (2014). "Spin current generated by thermally driven ultrafast demagnetization." Nature communications 5: 4334.

5. "Surface magneto-optic Kerr effect." Review of Scientific Instruments 71(3): 1243-1255.

6. Bergeard, N., et al. (2016). "Hot-electron-induced ultrafast demagnetization in Co/Pt multilayers." Physical review letters 117(14): 147203.

CHAPTER 6
Conclusion

In this work I have presented the pump-probe instrumentation system, which I installed for highly sensitive time domain thermoreflectance (TDTR) and time-resolved magneto optic Kerr effect (TR-MOKE) measurements. By modulating the Ti:Sapphire's innate 80MHz repetition rate with an overlaying 10.7MHz frequency, via an electro optic modulator (EOM) I was able to lock in to the AC response of the pump laser heating via an SRS lock-in and a computer lock-in. Using a variety of laser setups (Front Front, Front Back, red red and red blue), I was able to conduct a medley of experiments as a function of position and wavelength with noise near the Shot noise level.

I then investigated the longitudinal spin dependent Seebeck effect (LSSE) in Au/Iron Garnet bilayer systems using the aforementioned pump-probe laser system. Using TDTR and TR-MOKE as a function of wavelength and iron garnet, I was able to obtain the electron and phonon coupling in the 60nmAu layer as well detect the spin accumulation in the Au due to a spin current emanating from the magnetic insulator interface. With these experiments I obtained an electron-phonon coupling of $2 \cdot 10^{16} W/m^3 K$ and a SSE coefficient for Au/TmIG on the order of $1 \cdot 10^8 A/m^2 K$.

To serve as a resource describing the electron and phonon contributions to Au's thermoreflectance I took advantage of the band structure of Au in being able to access intraband or interband transitions by varying the probe energy used in TDTR measurements on 60nmAu/Sapphire. By doing so I obtained the α and β sensitivity scaling factors for the electron and phonon contributions to the thermoreflectance. This allowed me to conduct heat transfer measurements on more complex AuCoML systems as well as serve as a resource for future works.

Next we studied heat transfer in Au/AuCo multilayer samples. By taking advantage of the wavelength dependent TDTR measurements on 60nmAu/Sapphire, I was able to apply the temperature evolution of electrons and phonons into a hybridized transport model describing heat transport in Au/AuCoML nanoscale metal systems. Using several TDTR and TR-MOKE measurements as a function of position and probe energy, I was able to fit my experimental data with no free parameters, other than the ballistic length of 60nm. This modified diffusive model (so called super-diffusive) is in good agreement with all 3 of my experimental results regardless of experimental type (TDTR vs TR-MOKE), position, (probe Au or probe AuCoML), or probe energy.

I also used the pump-probe system to condcut wavelength dependent and thickness dependent spin accumulation measurements in Au due to demagnetization of a Au Co multilayer. I performed as a function of Au thickness as well as probe energy via TR-MOKE measurements. These measurements serve to describe the Kerr signal while serving as a resource to future works regarding maximizing signal or in characterizing obtained results as my results a show a high dependence of magnitude of Kerr signal and sign of signal with respect to probe energy.

I accomplished these tasks using robust experimental techniques that I developed. Specifically, I present methods for investigating unknown material properties that are extremely challenging to measure.